Transport Modeling of Industrial Ventilation

by

Kyle D. Squires

Prepared with Support from the
National Institute for Occupational Safety and Health
Grant Number R01 OH03052

Report TM-4

Department of Mechanical Engineering
University of Vermont
Burlington, Vermont 05405

June 1997

Contents

1 Significant Findings

The focus of work performed under Grant R01 OH03052 was development of new computational models appropriate for predicting contaminant transport in the complex turbulent flows encountered in industrial ventilation applications, with an emphasis on contaminants comprised of dense particulates. The newly developed model are based on large eddy simulation (LES), a more accurate technique for predicting turbulent transport than methods currently used in engineering practice. The goal of this work was to extend LES to prediction of turbulent flows transporting small particles which do not follow the flow and to validate the model against experimental measurements from well-defined test problems.

Overall, one of the most significant findings from this work is that out model is an accurate method for *predicting* particulate transport in the complex turbulent flows encountered in industrial ventilation applications. Because it is based on LES, the model requires considerably less empiricism than existing methods. The accurate performance of the model is significant since current methods can be considered, at best, "post-dictive", i.e., capable of predicting only those problems on which the model was calibrated. LES is substantially more robust and can accurately predict a wide range of complex phenomena, e.g., vortex shedding around a worker and particle deposition onto a surface, two very different problems with completely different physical features.

In this study, we showed that LES can reproduce the complicated statistical features of particle transport measured in experiments, e.g., accurate prediction of mean and fluctuating particle velocities and concentrations. More importantly, we also found that LES can accurately predict the complex structural features of particle transport in turbulent flows. It has been well documented that aerosol concentrations in turbulent flows are highly non-uniform, with peak concentrations as much as 20-40 times the global mean value! This preferential concentration results from particle interactions with turbulent eddies which are the same as occur, for example, in the flow pattern around a worker near a local exhaust device. This poses significant health risks since instantaneous exposures to workers can be substantially larger than estimates typically obtained using personal samplers, which provide only a time-weighted average and can only indirectly account for large excursions from the mean.

2 Usefulness of Findings

The long-range objective of our research is development of accurate and reliable methods for predicting airflow patterns and contaminant transport in the flow fields encountered in industrial ventilation applications. The ultimate goal is to develop a new generation of computational models which may be used by health professionals in design and evaluation processes. A flexible computational tool would provide substantially more accurate estimates of worker exposure to suspended contaminants.

Computational modeling of contaminant transport is difficult since the flow fields encountered in ventilation applications are time-dependent, three-dimensional, and turbulent. The particular interest of this study was on applications in which the contaminant is comprised of dense particulates which do not follow the underlying carrier flow. For these flows, existing models are inadequate due to both deficiencies associated with prediction of the turbulent gas flow as well as inaccurate particle dispersion models.

The complex nature of transport in ventilation problems in turn complicates design. For the most part, there are only general guidelines for design of ventilation devices. There does not exist, for example, any well-developed rationale for current design practices and, consequently, design techniques applicable to large classes of ventilation systems are not available. The complexity of the flow fields associated with ventilation devices had lead to an inadequate understanding of the contaminant transport processes in these three-dimensional, turbulent flow fields. Accurate models are important, however, since they would allow estimation of exposure for variations in geometry, flow rate, and type of contaminant, among other variables. Accurate models would then help eliminate much of the costly experimentation currently needed to ensure worker health and safety in the workplace.

In this study the foundation was established for a new generation of computational models which will ultimately comprise a key component for use in design and analysis by health professionals. This foundation has been established by by first developing the basic computational model and then validating it using test problems which possess the same complex physical features as encountered in practice. The significant findings of this study and summarized in the previous section have substantially advanced our models for prediction of the complex turbulent flow fields encountered in the workplace. Based upon the findings and successful completion of this study, future efforts should focus on applying LES to complex configurations more representative of those encountered in the workplace. Two examples are prediction of the flow around a worker near a local ventilation device and modeling transport in confined spaces. The purpose of such studies would be to validate our model in flows more complex than considered in our previous work. Such an investigation would bring into focus the entire computational approach and would allow us to explore issues relevant to not only accurate physical modeling of contaminant transport, but also the computational issues, e.g., solution algorithms, computational platforms, etc., which must be resolved before a working model can be used by health professionals.

3 Abstract

Modeling contaminant transport in industrial ventilation applications is difficult because the flow fields encountered are time-dependent, three-dimensional, and turbulent. For contaminants comprised of dense particles or droplets, previous studies have shown that interactions between particles and turbulent eddies result in locally large concentrations, as much as 20-40 times the global mean value. These interactions are often established by the presence

of a worker near a local exhaust device. Consequently, suspended particulates may pose significantly greater health risk to workers than has been previously thought. Computational models present a powerful tool for assessing the risk posed by suspended particles. Unfortunately, current models are unable to accurately account for the complex interactions between particles and turbulence and therefore new approaches are needed. Because of the development of dynamic subgrid-scale turbulence models, large eddy simulation has emerged as a powerful approach for predicting complex flows, but without requiring *ad hoc* calibration of model constants. Consistent with our long-term objective in developing of reliable predictive methods for modeling transport in industrial ventilation applications, the purpose of this investigation was to develop and validate new computational models based on LES for predicting particulate transport.

The computational technique was based on large eddy simulation of the filtered Navier-Stokes equations. The equations governing conservation of mass and momentum for an incompressible fluid were solved using the fractional step method on a staggered grid. Second-order central differences were used to discretize spatial derivatives, the discrete system was time-advanced using mixed explicit/implicit scheme (second-order Adams-Bashforth for the convective terms and Crank-Nicholson for the linear terms). The subgrid-scale stress in the momentum equations was closed using the Smagorinsky eddy viscosity model. The coefficient in the Smagorinsky model was calculated using the dynamic procedure outlined in Germano *et al.* (1991) and Meneveau *et al.* (1996). Following development of the solution method for the carrier flow, particle tracking capabilities were incorporated into the computer code. The equation of motion used in this work included nonlinear drag and gravitational drift and is appropriate to describing the motion of a spherical particle in a nonuniform, gas-phase turbulent carrier flow. A series of interpolation schemes were tested and it was found that fourth-order accurate Lagrange polynomials accurately recovered fluid velocities at particle positions.

LES predictions of several particle-laden flows were evaluated using both experimental measurements and results from direct numerical simulation. A wide array of test problems were considered, including prediction of particle deposition onto the wall of a turbulent boundary layer, particle transport in fully-developed channel flow, and prediction of a high Reynolds number particle-laden mixing layer. Reynolds numbers in the carrier phase varied from 3,300 in the channel (based on centerline velocity and channel half-width) to over 20,000 in the mixing layer (based on the velocity difference across the layer and vorticity thickness), a range covering the Reynolds numbers encountered in ventilation applications. Aerodynamic diameters considered in the simulations and were in the inspirable range. The actual values were chosen the same as in the available experimental measurements, ranging from 30 to 130μm. LES predictions compare favorably with experiments, predicting the enhanced particle fluctuating velocities with increasing response time in boundary layers and the increased lateral dispersion in the mixing layer. Significantly, LES also predicts the complex structural features of particle-laden turbulence, i.e., preferential concentration

of particles into regions of high strain rate. Both qualitative and quantitative measures of preferential concentration are in good agreement with experimental measurements and results from direct numerical simulation.

4 Body of Report

4.1 Background

4.1.1 Motivation

An issue of primary importance to industrial health and hygiene is control of worker exposure to air-borne contaminants. One method of reducing worker exposure to contaminated air is obtained through the use of local exhaust devices such as ventilation hoods. Ventilation hoods are designed to withdraw enough of the contaminated air such that employee overexposure is avoided. Therefore, accurate design and development of these devices is critical in maintaining employee health and safety in the workplace.

For the most part, design of ventilation hoods has been based on empirical evidence obtained from experimental measurements (e.g., see Dalla Valle & Hatch 1932, Dalla Valle 1952, Silverman 1942a,b, Baturin 1972, Flynn & Ellenbecker 1987, Conroy *et al.* 1988, Flynn & Ljungqvist 1995). These and other efforts have resulted in general guidelines for hood design. However, other than these empirical studies, there is no well-developed rationale for current design practices and, consequently, design techniques applicable to large classes of ventilation systems are not available. This is due in part to the complexity of the flow fields associated with ventilation devices and the inadequate understanding of the contaminant transport processes in these three-dimensional, turbulent flow fields.

An area especially poorly understood is transport in unsteady flow fields in which the contaminant is comprised of dense particulates. The hazard posed by particulates to the worker may generally be classified in terms of particle aerodynamic size. Of interest in this work are hazards posed by inspirable particulates, i.e., particles with diameters $\leq$ 50–100μm . Particles in this size range are of extreme importance in occupational health though, they are at the upper end of inspirability (see Phalen *et al.* 1986, Breysse & Swift 1980). If they are also soluble, these particles represent a significant health hazard since they will be rapidly absorbed into the blood stream. Most industrial particle distributions are highly skewed based on mass distribution (Hinds 1982). Thus, particles in the 50 to 100μm range would be expected to contribute a very high proportion of the total body burden of the specific contaminant. Such a contribution to body burden becomes a significant health risk when it involves a soluble aerosol such as beryllium, lead, arsenic, organophosphates, etc. since, although the particles do not penetrate into the pulmonary spaces, they are readily absorbed directly into the blood stream from either the nasal mucosa or the gastro-intestinal track and proceed to the specific target organ (Doull *et al.* 1980, Moss & Kanapilly 1980).

Flow field unsteadiness in ventilation applications can result from interactions between the

worker (or other obstacles) and the air flow induced by the exhaust hood. In particular, the presence of the worker can actually induce large-scale turbulent unsteadiness in the vicinity of the worker's breathing zone. These motions, i.e., large-scale turbulent vortices, have a very significant effect on the processes which govern particle transport in and around the worker. Previous work has shown that these turbulent motions can have a profound effect on particle motions and concentration fields. The organized motions present in turbulent flows, e.g., the large-scale vortices shed from obstacles, significantly influence particulate transport. Both experiments (e.g., see Kobayashi *et al.* 1988, Lazaro & Lasheras 1992a,b, Longmire & Eaton 1992, Hishida *et al.* 1992, and Flynn & Ljungqvist 1995) and computations (Squires & Eaton 1991) have demonstrated that these organized motions can greatly increase instantaneous particle concentrations over field-averaged values. This increase in particle concentration results from a bias in the particle trajectory towards regions of low vorticity and high strain rate. It is precisely the organized motions in the flow which induce the bias in particle motion.

There are several important consequences of preferential concentration of particles into (hydrodynamically) preferred regions of the flow. Directly relevant to occupational health and safety in the workplace is that it is likely there are many applications in which instantaneous contaminant concentrations in the worker's breathing zone could be significantly greater than allowable exposures, even though the average concentration in the surrounding atmosphere is well below allowable levels. Since the effects of turbulent unsteadiness are induced by the *presence* of the worker, the regions of locally large particulate concentrations will also be found near the worker's breathing zone and would be anticipated to move with the worker or be re-established as the worker moves about in the velocity field. The consequence of this is that the worker could be exposed to hazardous levels exceeding STEL's or PEL's, depending on associated aerodynamic diameters and levels of vorticity. Ventilation systems based on conventional design criteria will not necessarily maintain low levels of particulate concentrations near the worker. It is also important to point out that it is not necessarily the mean concentration which is the relevant parameter for determining worker exposure; rather, it is the deviation from the mean and duration of exposure to high concentrations which may be more important from the standpoint of worker safety. Such deviations would be especially important near the worker's head and may not be detected using low-flow (< 2 Lpm) personal samplers at chest level. Current design criteria for ventilation systems are unable to account for the complicated interactions between particles and the underlying turbulent air flow; therefore, more refined approaches are needed.

4.1.2 Modeling

One approach that can provide the detailed information required for improved design of ventilation systems is the use of numerical modeling. Numerical predictions of the flow fields associated with local exhaust devices are useful both as a means of understanding the basic mechanisms governing the flow as well as ultimately providing a flexible tool for

design and analysis. Much of the previous computational work related to analyzing flow fields associated with exhaust hoods has been performed under the assumption that the flow is incompressible, inviscid, irrotational, and, with few exceptions, two-dimensional (e.g., see Flynn & Ellenbecker 1985, Garrison & Wang 1987, Flynn & Miller 1989, Garrison & Park 1989, Anastas & Hughes 1989, and Anastas 1991). Under these assumptions the velocity field may be expressed as the gradient of a potential function which in turn satisfies Laplace's equation. In most of these previous studies the principal emphasis has been on matching computational results to experimentally measured velocity characteristics along the centerline of the hood or in the vicinity of the hood face. Unfortunately, the assumptions implicit in these methods, e.g., inviscid, irrotational flow, prohibit them from being applied to study the time-dependent effects and interactions between a turbulent fluid and suspended particles. It is important to point out that vortex methods have also been used for modeling flow fields in ventilation applications (e.g., see Flynn & Miller 1991). While vortex methods can provide a reasonable description of large scale motions, the methods have been applied to only two-dimensional geometries. Extension to three-dimensional simulations remains difficult.

To examine particulate interactions in turbulent flow fields more general methods than either potential flow analyses or vortex methods need to be employed. Since the effects of turbulence can often be the controlling factor in these flows, numerical schemes must accurately represent turbulent fluid motions. However, accurately modeling turbulence has proven to be perhaps the most challenging aspect of computational fluid dynamics. Due to the complex nature of turbulence, various hierarchies of numerical simulation have emerged. The most fundamental level of computation is direct numerical simulation (DNS). In DNS the governing equations are solved without resorting to turbulence modeling of any kind. Therefore, in DNS the entire spectrum of turbulent motions is resolved directly. The results from DNS can then be analyzed in much the same way as those obtained from laboratory experiments. DNS has been a powerful tool, capable of providing a great deal of information on canonical turbulent flows such as flat-plate boundary layers and fully-developed turbulent channel flow (Spalart 1986 and Kim *et al.* 1987). DNS has also been successfully applied to studies of particle-laden turbulence (Squires & Eaton 1990, 1991a,b). Unfortunately, because the range of length scales increases dramatically for increasing values of the Reynolds number (Tennekes & Lumley 1972), DNS is only applicable to low Reynolds number canonical flows. To examine particulate interactions with turbulent flows at realistic Reynolds numbers, the effects of turbulence must be represented indirectly.

One approach to computation of turbulent flows for realistic applications is obtained through solution of the time-averaged governing equations. In this approach the effects of turbulence are represented by solving additional equations for the transport of quantities such as the turbulence kinetic energy and dissipation rate (i.e., the K-ε model). The K-ε model is among the most widely used methods of representing the effects of turbulence in computations of engineering and scientific interest. The principal deficiency with the

model, however, is that it attempts to represent the entire spectrum of turbulent velocity fluctuations using a reduced set of equations with a number of adjustable constants. The constants are not universal and must be adjusted in an *ad hoc* manner in order to obtain accurate predictions of different classes of flows (see Rodi 1980). Computations performed using the K-ε model also provide only a time-averaged prediction of the flow field. Therefore, these computations are inappropriate for examining instantaneous properties of the flow, e.g., maximum particulate concentrations in the worker's breathing zone.

4.1.3 Large Eddy Simulation and Dynamic Subgrid Modeling

A more accurate approach to modeling particle interactions with turbulence is obtained through the use of large-eddy simulation (LES). In LES the governing equations are filtered (i.e., volume averaged) to yield transport equations for the large-scale variables. Volume-averaging the governing equations yields correlations between small scale quantities (i.e., subgrid-scale stresses) which must be modeled in terms of the computed variables. The principal advantage of LES over the time-averaged methods is that a large fraction of turbulent motions are computed directly, i.e., without resorting to any turbulence modeling. A basic tenet of turbulence research is that the small-scale motions are more isotropic and universal in character than the large-scale motions (Tennekes & Lumley 1972). Therefore, it should be possible to parameterize these motions using simpler and more universal models than those employed in computational methods in which the governing equations are time averaged. In fact, one of the most successful subgrid-scale models used to date is that proposed originally by Smagorinsky (1963). Smagorinsky formulated an eddy viscosity model much simpler in form than many of the modeling approaches used in current K-ε computations. The principal limitation in the use of LES as a tool for prediction of turbulent flows of engineering interest, however, has been much the same as that associated with time-averaged computations. This limitation has been due to the fact that nearly all previous LES results have required *ad hoc* specifications of subgrid-scale model coefficients to obtain good agreement with laboratory measurements. This has constrained predictions obtained using LES to rather narrow classes of flows.

Many of the deficiencies associated with previous subgrid-scale modeling efforts were remedied by the work of Germano *et al.* (1991). Briefly, these investigators recognized that because the large-scale field in LES is computed directly, a large amount of information regarding the structural interactions of the turbulence is available as part of the computation. The advance gained by Germano *et al.* was utilization of this information in formulation of the subgrid-scale model. Using an algebraic identity developed by Germano (1992), they formulated an eddy viscosity model for the subgrid-scale stresses in which an expression for the model coefficient is obtained as a function of the local flow properties. Computations of transitional and fully-developed turbulent channel flow using this concept showed very good agreement with direct simulation data. The concept developed by Germano *et al.* for simulations of incompressible flows has since been extended to LES of compressible

turbulence by Moin *et al.* (1991) and tested in a wide range of other complex flows (e.g., see Wu & Squires 1997). Good agreement between LES predictions and experimental results have been obtained in these and other studies. It should again be emphasized that *ad hoc* calibration of the model coefficients is not required. LES results obtained in these studies were as good or better than previous LES computations in which model constants had been calibrated to improve agreement between simulation and experiment. These developments in subgrid-scale modeling have made viable the use of LES as a tool for application to the flow fields associated with ventilation systems. In fact, LES has been defined by the National Research Council as *"the only hope we have to detail flow models of real-world engineering complexity"*, [*Research Directions in Computational Mechanics*, Vol. 1, National Research Council (1991)].

Though LES has recently made major breakthroughs in calculation of single-phase flows, it has seen relatively few applications to prediction of particle-laden turbulence. LES would appear an ideal candidate for particle-laden turbulence because a large fraction of turbulent motions are directly computed, a model is only required to represent particle transport by subgrid velocities. Since the subgrid motions possess significantly less energy than the large scales of motion, errors in particle-transport subgrid models should have a substantially smaller effect on the overall predictive accuracy as compared to other techniques (e.g., K-ε where the entire spectrum of fluctuations on particle motion must be specified). One of the major goals of this work was to explore the predictive accuracy of LES for particle-laden turbulence and establish a foundation for future applications to the flows encountered in industrial ventilation problems. Such an effort is crucial to the success of subsequent research directed at incorporation of additional complexity into computational methods used to predict the flow fields associated with ventilation systems. Because of the complex physics present in these flow fields it is preferable to develop and validate models in calculations of a series of well-defined "building block" flows, rather than consider development of a general computational algorithm suitable for arbitrary ventilation applications.

4.2 Specific Aims

1. **Translation of an existing computer code from a high-level vector programming language (Vectoral) to Fortran.** This code is used for simulation of the time-dependent, compressible Navier-Stokes equations (three-dimensional). The Vectoral programming language is currently only available at the NASA-Ames Research Center. Translation of the code is necessary in order to improve portability.

2. **Incorporation of particle tracking capability into the code.** Included in this effort is the development of the necessary interpolation schemes as well as implementation of the particle equation of motion appropriate for this study.

3. **Development of particle transport models.** In this study the technique of large eddy simulation shall be employed for computation of the gas flow. Because of the

relatively large amount of information regarding the properties of the computed large-scale field, emphasis at this stage of the research is on development of transport models appropriate for LES.

4. **Validation of the models developed in item (3) using large-eddy simulation of particle dispersion in temporally-evolving free shear layers.** Model predictions will be tested using the experimental measurements of Lazaro & Lasheras (1992a,b) and Hishida *et al.* (1992). The measurements obtained by these investigators will permit detailed analysis of the accuracy and reliability of the transport models. A critical issue to be resolved at this stage of the research will be the ability of newly-developed transport models to predict the preferential concentration of particles in regions of low vorticity and high strain rate. While preferential concentration has been documented experimentally and also observed in direct numerical simulations, existing transport models are unable to reflect this important phenomenon. Thus, the model development will undergo substantive validation through the use of existing data sets.

4.3 Procedures and Methodology

4.3.1 LES of the Incompressible Navier-Stokes Equations

Specific Aim 1:

The model developed in this study is based on LES of the incompressible Navier-Stokes equations. It should be noted that a slight modification to the means by which Specific Aim 1 was accomplished significantly improved the overall efficiency in meeting the goals and objectives of the work. It was originally forecast that translation into Fortran of a computer code for simulation of the compressible momentum equations would be the most efficient means of completing Specific Aim 1. However, our group developed a numerical method for solution of the incompressible Navier-Stokes equations as part of another project in LES (Wu et al. 1995). Code development in that area proceeded exceedingly well and therefore we adapted that numerical approach for use in this study. Thus, while the overall objective of Specific Aim 1 remained the same–development of a numerical method for the Navier-Stokes equations–the method used in this work was applied to the incompressible momentum equations. It is important to emphasize that solution of the incompressible Navier-Stokes equations did not limit in any way the scope of this work and, in fact, permitted a more timely completion of the project. Development of the numerical method, i.e., achievement of Specific Aim 1, is described in this subsection.

In LES the dependent variables are decomposed into a large scale (i.e., resolved) component and subgrid-scale contribution. The large scale variables, denoted using an overbar, are formally defined by a filtering operation,

$$\overline{f}(\mathrm{x}) = \int_D f(\mathrm{x}')\overline{G}(\mathrm{x},\mathrm{x}')d\mathrm{x}', \tag{1}$$

where D is the computational domain and $\overline{G}$ is the filter function. Application of the filtering operation to the incompressible Navier-Stokes equations yields the equations governing the motion of the resolved scales,

$$\frac{\partial \overline{u}_{1,j}}{\partial x_j} = 0\,, \tag{2}$$

$$\frac{\partial \overline{u}_{1,i}}{\partial t} + \frac{\partial}{\partial x_j}(\overline{u}_{1,i}\overline{u}_{1,j}) = -\frac{1}{\rho_1}\frac{\partial \overline{p}_1}{\partial x_i} + \nu_1 \frac{\partial^2 \overline{u}_{1,i}}{\partial x_j \partial x_j} - \frac{\partial \tau_{1,ij}}{\partial x_j}\,. \tag{3}$$

In (2) and (3), $\overline{u}_{1,i}$ is the fluid velocity, $\overline{p}_1$ is the fluid pressure, ρ_1 and ν_1 are the density and kinematic viscosity of the fluid, respectively. The indices $i = 1, 2, 3$ refer to the x (streamwise), y (cross-stream), and z (spanwise) axes, respectively, and an overbar, $\overline{\cdot}$, denotes application of the filter.

The effect of the subgrid scales on the resolved eddies in (3) is represented by the SGS stress, $\tau_{1,ij} = \overline{u_{1,i}u_{1,j}} - \overline{u}_{1,i}\overline{u}_{1,j}$. In this study $\tau_{1,ij}$ is parameterized using an eddy viscosity hypothesis,

$$\tau_{1,ij} - \frac{1}{3}\delta_{ij}\tau_{1,kk} = -2\nu_T \overline{S}_{1,ij}\,, \tag{4}$$

where the eddy viscosity is,

$$\nu_T = C\overline{\Delta}^2 |\overline{S}_1|\,, \tag{5}$$

the resolved-scale strain rate tensor is defined as

$$\overline{S}_{1,ij} = \frac{1}{2}\left(\frac{\partial \overline{u}_{1,i}}{\partial x_j} + \frac{\partial \overline{u}_{1,j}}{\partial x_i}\right)\,, \tag{6}$$

and $|\overline{S}_1| = \sqrt{2\overline{S}_{1,ij}\overline{S}_{1,ij}}$ is the magnitude of $\overline{S}_{1,ij}$. The filter width $\overline{\Delta}$ is defined as $\overline{\Delta} = \left(\overline{\Delta}_1\,\overline{\Delta}_2\,\overline{\Delta}_3,\right)^{1/3}$ where $\overline{\Delta}_1$, $\overline{\Delta}_2$, and $\overline{\Delta}_3$ are the grid spacings in the x, y, and z directions, respectively. The model coefficient C in (5) requires specification in order to close the system (2) and (3).

Unlike previous applications in which the model coefficient was determined *a priori* and then adjusted from flow to flow, in this research the coefficient C was determined dynamically using the resolved velocity field. Following Germano *et al.* (1991), a second filter, the test filter (denoted using $\widehat{\cdot}$), is introduced to derive an expression for C. Germano (1992) showed that the resolved turbulent stress,

$$L_{1,ij} = \widehat{\overline{u}_{1,i}\overline{u}_{1,j}} - \widehat{\overline{u}}_{1,i}\widehat{\overline{u}}_{1,j}\,, \tag{7}$$

the SGS stress $\tau_{1,ij}$, and the subtest-scale stress $T_{1,ij} = \widehat{\overline{u_{1,i}u_{1,j}}} - \widehat{\overline{u}}_{1,i}\widehat{\overline{u}}_{1,j}$ are related by,

$$L_{1,ij} = T_{1,ij} - \widehat{\tau}_{1,ij}\,. \tag{8}$$

Assuming that a closure similar to (4) may be used to model the test-field stress $T_{1,ij}$, it is possible to use (8) to derive an expression for C. Lilly (1992) used a least-squares approach to solve the resulting system of equations for the model coefficient C. For a flow with two

statistically homogeneous directions (x and z) as in the flows considered in this study, an "average" coefficient is obtained as,

$$C(y,t) = -\frac{1}{2}\frac{\langle L_{1,ij} M_{1,ij} \rangle_{xz}}{\langle M_{1,kl} M_{1,kl} \rangle_{xz}} , \tag{9}$$

where,

$$M_{1,ij} = \widehat{\overline{\Delta}}^2 \widehat{||\overline{S}_1||\overline{S}_{1,ij}} - \overline{\Delta}^2 \widehat{|\overline{S}_1||\overline{S}_{1,ij}} . \tag{10}$$

In (10), $\langle\ \rangle_{xz}$ denotes averaging over x-z planes. Averaging the numerator and denominator of (9) are required in order to avoid large local variations in C as well as negative values which cause numerical instability. Thus, as shown in (9) the coefficient is a function of distance from the wall and time (see Ghosal *et al.* 1995 and Meneveau *et al.* 1996 for further discussion). The only parameter needed to be specified in the dynamic model is the ratio between the test filter width, $\widehat{\overline{\Delta}}$, and grid scale filter width $\overline{\Delta}$. As has been shown by Germano *et al.* (1991), LES results are not overly sensitive to this ratio and in this work $\widehat{\overline{\Delta}}/\overline{\Delta} = 2^{2/3}$ was used. Test filtering in the streamwise and spanwise directions was typically carried out in Fourier space using a sharp cut-off filter.

A different approach to determining C was developed by Meneveau *et al.* (1996) and used in some of the model evaluations performed in this research. In Meneveau *et al.* (1996), the error in (8) is minimized along fluid particle trajectories, resulting in an expression for the model coefficient of the form,

$$C(\mathbf{x},t) = \frac{I_{LM}}{I_{MM}} . \tag{11}$$

In principle, I_{LM} and I_{MM} are obtained from the solution of separate transport equations. However, to reduce the computational cost associated with calculation of C, the numerator and denominator of (11) are obtained using a simple time discretization, resulting in

$$I_{LM}^{n+1}(\mathbf{x}) = H\{\epsilon L_{1,ij}^{n+1} M_{1,ij}^{n+1}(\mathbf{x}) + (1-\epsilon) I_{LM}^{n}(\mathbf{x} - \overline{u}_{1,i}^{n}\Delta t)\} , \tag{12}$$

$$I_{MM}^{n+1}(\mathbf{x}) = \epsilon M_{1,ij}^{n+1} M_{1,ij}^{n+1}(\mathbf{x}) + (1-\epsilon) I_{MM}^{n}(\mathbf{x} - \overline{u}_{1,i}^{n}\Delta t) , \tag{13}$$

where $H\{x\} = max(x,0)$ is the ramp function, the timescale in (13) is defined as $T = 2\Delta I_{LM}^{-1/4}$, and

$$\epsilon = \frac{\Delta t/T^n}{(1+\Delta t/T^n)} . \tag{14}$$

The numerical scheme used to solve the equations governing conservation of mass and momentum is based on the fractional step (see Kim & Moin 1985, Wu *et al.* 1995). Spatial derivatives are expressed using second-order accurate central differences on a fully staggered grid. The continuity equation (2) was enforced about the pressure nodes in each cell and the momentum equation (3) was satisfied about the velocity nodes. Time advancement of the discrete equations is based on block-LU decomposition of the fully discretized system. To avoid the stability restriction imposed by the viscous terms an implicit time advance scheme was applied. Second-order Adams-Bashforth was used for advancement of the convective

terms and part of the SGS term while the Crank-Nicholson method was applied for update of the viscous terms and a portion of the SGS stress. The Poisson equation for pressure was solved using series expansions in the streamwise and spanwise directions together with tridiagonal matrix inversion (e.g., see Williams 1969, Kim & Moin 1985).

4.3.2 Treatment of the Particles

Specific Aim 2:

Following development of the Navier-Stokes solver for numerical solution of the LES equations described in the previous section (Specific Aim 1), the three primary tasks of Specific Aim 2 were to incorporate the particle equation of motion into the code, implement an accurate scheme for interpolation of gas properties to the particle position, and determine sample sizes necessary for accurate computation of particle statistics. The three components of Specific Aim 2 were completed on or ahead of schedule and are described in this section.

Particle motion was determined through solution of the equation describing the motion of a sphere in an unsteady, nonuniform velocity field. For particles with density ρ_2 much larger than that of the fluid ρ_1 the forces on the sphere reduce to the drag term and gravity,

$$\rho_2 \frac{du_{2,i}}{dt} = -\rho_1 \frac{3}{4} \frac{C_D}{d} |\mathbf{v}_r| v_{r,i} + \rho_2 g_i \,, \tag{15}$$

where $u_{2,i}$ is the particle velocity, d the particle diameter, $v_{r,i} = u_{2,i} - u_{1,i}$ the relative velocity between particle and fluid, $|\mathbf{v}_r| = |v_{r,i} v_{r,i}|$ is the magnitude of the slip velocity, and the acceleration of gravity is g_i. The drag coefficient C_D is expressed in terms of the particle Reynolds number Re_p as,

$$C_D = \frac{24}{Re_p} \left[1 + 0.15 Re_p^{0.687} \right] , \qquad Re_p = \frac{|\mathbf{v}_r| d}{\nu_1} . \tag{16}$$

It should be noted that (15) is appropriate for describing the motion of smooth rigid spheres and neglects the influence of virtual mass, buoyancy, and the Basset history force on particle motion. For particles with material densities large compared to the fluid these forces are negligible compared to the drag. Given the fluid velocity $\overline{u}_{1,i}$ along the particle trajectory, (15) is integrated in time using second-order Adams-Bashforth. Particle displacements were also integrated using the second-order Adams-Bashforth method.

Since it is only by chance that a particle is located at a grid point where the Eulerian velocity field is available, interpolation is required to obtain the fluid velocity at the location of the particle. Investigations of the interpolation schemes necessary for accurate resolution of velocity autocorrelations, mean-square dispersion, and particle velocities were examined using turbulent channel flow. As may be observed in Figure 1, unacceptable errors in the autocorrelation arise using low-order methods such as linear interpolation. The effect of the interpolation scheme on the mean flow was found to be small. However, the fluid fluctuating velocities were sensitive to the interpolation method as shown in Figure 2. As can be observed in the figures, greater accuracy than can be obtained using linear interpolation is necessary for

accurate resolution of the fluctuating velocities. Figure 2 shows the turbulent fluctuations are well resolved using Fourth-order accurate Lagrange polynomials. For the model tests presented below, interpolation was performed using Fourth-order Lagrange polynomials.

The effect of sample size on quantities such as the single-particle velocity autocorrelation is shown in Figure 3. As shown in the figure, single-particle statistics in turbulent shear flows are accurately resolved using approximately 5000 particles. Other statistics such as the mean and fluctuating particle velocities calculated by averaging over the domain require substantially larger sample sizes. Figures 4 and 5 shows that the mean and fluctuating velocities can be accurately resolved using 250,000 particles, i.e., an average of about 1 particle per cell.

4.3.3 Transport Models

Specific Aim 3:

In Specific Aim 3 the goal was to develop particle transport models appropriate for large eddy simulation. In LES the smallest scales of motion are not resolved by the computational grid, only their effect on the large eddies is represented via the SGS model. Thus, when considering particle transport only the large-scale velocity fluctuations are directly available in an LES computation for determining particle motion. Transport models for LES were successfully constructed in this phase of the work and Specific Aim 3 was completed on schedule.

Work in achievement of Specific Aim 3 initially focused on development and incorporation of models for subgrid-scale kinetic energy, q^2, into the LES. The SGS kinetic energy was then used to scale the fluid velocity fluctuations along the particle trajectory. In particular, models were constructed in which the fluid velocity in the particle equation of motion was the resolved component $\overline{u}_i$, directly available in the LES, plus a subgrid component u_i'. The magnitude of the SGS fluctuation u_i' was determined by solving an additional transport equation for SGS kinetic energy, q^2. The transport equation used for determination of q^2 was that proposed by Schumann (1991), i.e.,

$$\frac{\partial q^2}{\partial t} + \overline{u}_j \frac{\partial q^2}{\partial x_j} = 2\nu_T |\overline{S}_1|^2 + \frac{\partial}{\partial x_j}\left(\frac{1}{3} l_\Delta \sqrt{q^2/2} \frac{\partial q^2}{\partial x_j}\right) + \nu \frac{\partial^2 q^2}{\partial x_j \partial x_j} - \sqrt{\frac{1}{2}} c_\epsilon \frac{q^3}{l_\Delta} , \qquad (17)$$

where,

$$c_\epsilon = \pi \left(\frac{2}{3k_0}\right)^{3/2} , \qquad l_\Delta = min\left\{\overline{\Delta}, c_\epsilon y\right\} , \qquad (18)$$

with the Kolmogorov constant $k_0 = 1.6$. Solution of (17) yields the magnitude of the SGS kinetic energy throughout the flow. The SGS components $u_i'^2$ were then obtained from q^2 and specified to have the same relative magnitudes as the resolved-scale intensities. The component fluctuations u_i' were then scaled by random numbers sampled from a Gaussian distribution and added to $\overline{u}_i$ at the particle location. The complete velocity, i.e., $\overline{u}_i + u_i'$, was used in (15) to determine the particle velocity. A dynamic formulation for the SGS kinetic

energy proposed by Yoshizawa (1986) was also used in other tests, yielding results nearly identical to those obtained using the transport equation.

It was originally forecast that preliminary tests of the particle transport models developed in achievement of Specific Aim 3 would be tested using simulations of thermal dispersion in grid turbulence. Grid-generated turbulence decays with downstream distance in the experiment (increasing time in the simulations) and is therefore not statistically stationary. This aspect in turn complicates evaluation of the models. Therefore, models of SGS particle transport were tested in calculations of fully developed channel flow and a turbulent mixing layer. This modification to the achievement of Specific Aim 3 enhanced model development and did not limit in any way the scope of the research.

4.3.4 Description of Model Validation Tests

Specific Aim 4:

In the final phase of the project, the computational model was validated through extensive comparisons to experimental measurements and results from direct numerical simulations. It was originally planned to test model predictions using the experimental measurements of Lazaro & Lasheras (1992a,b) and Hishida et al. (1992) in particle-laden turbulent mixing layers. Because the prior Specific Aims were completed on or ahead of schedule, it was possible to consider not only the mixing layer, but also extraction of Lagrangian statistics in turbulent channel flow, particle deposition in turbulent boundary layers, effect of shear-induced lift on particle motion, and transport in fully developed channel flow. These additional cases provided an even more stringent test of the model across a broader range of flows. A series of manuscripts have been written summarizing these efforts (see page 32). Each of the tasks comprising Specific Aim 4 were completed as originally proposed. Results from the channel flow and LES of a particle-laden mixing layer will be presented in the next section since these two calculations provide a representative summary of the model and its capabilities.

The flow between parallel channels is one of the most well-defined turbulent shear flows (Figure 6). A pressure gradient is used to drive the flow to a statistical equilibrium. Periodic boundary conditions are applied in the streamwise and spanwise directions, while the no-slip condition is applied on the channel walls. An advantage of model testing in channel flow is the large number of previous studies, in both single- and multi-phase flow, which have established a baseline for evaluating model predictions. The mean and fluctuating fluid velocities are shown in Figure 7 and Figure 8, respectively. The calculations shown in the figure were performed at a channel flow Reynolds number of 180, based on friction velocity and channel half-width. Also shown in the figures are the direct simulation results of Kim *et al.* (1987). As can be seen in the figure, there is good agreement between LES predictions and the DNS results. In addition to the checks of the numerical method (see Wu *et al.* 1995), the calculations of the channel flow help to firmly establish the accuracy of the numerical approach and computation of the gas-phase carrier flow.

Models were also tested in LES of a particle-laden mixing layer. The mixing layer is

characterized by the merging of two co-flowing fluid streams having different velocities. The streams are usually separated by an impermeable object upstream of their confluence. Downstream of the confluence, the two streams exchange momentum as they come into intimate contact with one another (Figure 9). The mixing layer itself is defined by the region in which this merging process occurs. The layer grows in thickness downstream of the confluence due to both molecular and turbulent diffusion, though turbulent transport processes are much more significant in nearly all applications of practical interest. The large-scale vortices present in the mixing layer are representative of the large organized motions found in the flow fields generated by ventilation devices, especially those generated by vortex shedding in the vicinity of the worker.

Numerical simulation of turbulent mixing layers is simplified by considering the evolution of the layer in a reference frame translating at the convection speed of the layer (i.e., the average velocity of the high- and low-speed streams, see Figure 10). The resulting simplifications in boundary conditions and other computational constraints that arise from considering the temporally evolving mixing layer are considerable. In this work the temporal flow was used as a platform for model testing. It should be emphasized that simulations of temporally-evolving layers contain the relevant physics with regards to particle interactions with large-scale turbulent motions.

4.4 Results and Discussion

4.4.1 LES of particle-laden channel flow

Simulation Overview

In this phase of Specific Aim 4, simulations of particle-laden channel were used for the purpose of investigating the accuracy and predictive capability of the LES. The computations were performed for the same conditions as in the direct numerical simulations of Rouson & Eaton (1994) and experimental conditions considered by Kulick *et al.* (1994) and Fessler *et al.* (1994). The governing equations and numerical method have been described earlier.

The simulations were performed at Reynolds numbers based on friction velocity and channel half-width of 180 and 644 (corresponding to Reynolds numbers of 3,200 and 13,800 based on centerline velocity and channel half-width). At both Reynolds numbers the flow was resolved using $64 \times 65 \times 64$ grid points in the x, y, and z directions, respectively. The channel domain for the calculation at $Re_\tau = 180$ was $4\pi\delta \times 2\delta \times 4\pi\delta/3$ and $5\pi\delta/2 \times 2\delta \times \pi\delta/2$ at $Re_\tau = 644$. Previous computations of turbulent channel flow have shown these domain sizes are large enough to avoid contamination of the flow by periodic boundary conditions. The grid spacing in wall coordinates in the x and z directions was $\Delta x^+ = 35$ and $\Delta z^+ = 12$ at $Re_\tau = 180$ and $\Delta x^+ = 79$ and $\Delta z^+ = 16$ at $Re_\tau = 644$. A stretched grid was used in the wall-normal direction and for both Reynolds numbers the first grid point was at $y^+ < 1$.

Particle motion was governed by (15) and statistics of the particle cloud were obtained from the trajectories of 250,000 particles. The particles used in the simulations possess

material characteristics identical to those in the DNS study of Rouson & Eaton (1994) and experiments of Kulick *et al.* (1994) and Fessler *et al.* (1994): 28μm diameter Lycopodium particles, 25, 50, and 90μm diameter glass beads, and 70μm copper particles. The particle response time and radius a expressed in terms of both channel variables (δ and u_τ) and in wall units for the simulations at $Re_\tau = 180$ and $Re_\tau = 644$ are shown in Tables 1 and 2, respectively (the response time $\tau_p = \rho_p d^2/(18\nu\rho_f)$ shown in the table is the value corresponding to Stokes flow around the particle). The particle parameters at $Re_\tau = 644$ have been normalized by the experimental values of channel half-width $\delta = 20$mm and friction velocity $u_{1,\tau} = 0.49$m/s (see Kulick *et al.* 1994). The particle parameters in the DNS at $Re_\tau = 180$ were scaled by Rouson & Eaton (1994) to match the Stokes numbers defined in terms of the Kolmogorov timescale in the experimental measurements of Kulick *et al.* (1994). For both Reynolds numbers the particle radius is much smaller than the filter width except very near the wall where the particle radius can be comparable to the wall-normal grid spacing (the first grid point was at $y^+ = 0.45$ at $Re_\tau = 180$ and at $y^+ = 0.84$ at $Re_\tau = 644$). Thus, the effect of a nonuniform fluid velocity field on particle motion near the wall may be less accurately represented for the larger particles.

	28 μm Lycopodium	50 μm glass	70 μm copper
$\tau_p/(\delta/u_{1,\tau})$	0.048	0.65	4.50
τ_p^+	9	117	810
a/δ	0.00139	0.00277	0.00388
a^+	0.25	0.50	0.70

Table 1: Particle parameters in turbulent channel flow, $Re_\tau = 180$.

	28 μm Lycopodium	50 μm glass	90 μm glass	70 μm copper
$\tau_p/(\delta/u_{1,\tau})$	0.04	0.44	1.54	3.10
τ_p^+	26	283	992	1996
a/δ	0.0007	0.00125	0.00225	0.00175
a^+	0.450	0.805	1.449	1.127

Table 2: Particle parameters in turbulent channel flow, $Re_\tau = 644$.

From an arbitrary initial condition the Eulerian velocity field was time advanced to a statistically stationary state. The particles were then assigned random locations throughout the channel. The initial particle velocity was assumed to be the same as the fluid velocity at

the particle location. Particles were then time advanced in the flow field to a new equilibrium condition in which particle motion was independent of initial conditions. Similar to the fluid flow, statistics of the particle velocity were averaged over the two homogeneous directions, both channel halves, and time. Fluid statistics were averaged for $3.5\delta/u_{1,\tau}$ at $Re_\tau = 180$ and for $4\delta/u_{1,\tau}$ at $Re_\tau = 644$. The development time, i.e., the time required for particles to become independent of their initial conditions was larger for increasing values of the particle response time, e.g., $0.5\delta/u_\tau$ for the Lycopodium particles and $6\delta/u_\tau$ for the copper particles at $Re_\tau = 180$. After an equilibrium condition had been reached, particle statistics were accumulated for $6\delta/u_\tau$ at $Re_\tau = 180$ and $4.5\delta/u_\tau$ at $Re_\tau = 644$.

Statistical Features

The mean streamwise velocity profile obtained from the LES calculations is shown in Figure 11 for each particle type considered in the DNS (Fig. 11*a*) and experiments (Fig. 11*b*). Figure 11*a* shows that at $Re_\tau = 180$ there is good agreement between LES and DNS. As expected, both the LES and DNS show that the Lycopodium particles closely track the fluid flow. Near the wall ($y^+ < 10$) the Lycopodium velocity profile from the DNS slightly lags that of the fluid while the mean velocity from the LES is nearly equal to the fluid velocity. Rouson & Eaton (1994) attribute the lag in the Lycopodium profile to preferential concentration of Lycopodium particles in the low speed streaks. The discrepancy between LES and DNS results may be related to the fact that the near-wall structures are less well resolved in the LES and, consequently, preferential concentration of particles in low-speed regions is less significant than in the DNS, resulting in an over-prediction of the mean velocity of the Lycopodium particles (see §4.1 for further discussion). For the glass beads and copper particles the profiles in Figure 11*a* become increasingly larger than the fluid velocity for increases in the Stokes number. LES predictions of the mean velocity of 50μm glass beads are in good agreement with the DNS; the copper velocity profile from the LES calculations is also in good agreement with DNS results for $y^+ > 10$ but it may be observed from the figure that the DNS results are larger near the wall. Note also that both LES and DNS profiles of the copper particles exhibit a slight plateau near the wall. The plateau may result from the transport of high velocity particles from the outer region of the channel to the near-wall region and this feature appears to be somewhat more pronounced in the DNS. However, it is also important to note that the difference between LES and DNS is relatively small and confined to a very thin region near the wall.

Particle mean velocity profiles at $Re_\tau = 644$ from the LES calculations are shown in Figure 11*b* together with the experimental measurements for 50μm glass beads and copper particles from Kulick *et al.* (1994). Similar to the results at the lower Reynolds number, LES predictions show greater differences in the mean particle velocity relative to the fluid with increasing Stokes number; the largest differences occurring near the wall. As also observed at $Re_\tau = 180$, near the wall the Lycopodium particles slightly lead the fluid and are then nearly identical to the fluid velocity in the outer region. Comparison of the profiles for the 50μm glass beads demonstrates relatively good agreement for y^+ greater than about 20.

However, for $y^+ < 20$ the results in Figure 11*b* show that the experimental measurements increase towards the wall while LES predictions do not. It may also be observed that there is relatively poor agreement between the LES and Kulick *et al.* (1994) for the copper particles. For y^+ greater than roughly 10, the mean profile of the copper particles in the experiment is nearly equal to that of the fluid while in the LES the copper particles lead the fluid throughout the channel. As also apparent in Figure 11*b*, Kulick *et al.* (1994) found that the mean velocity of the copper particles increased substantially near the wall, an effect not observed in the LES at either Reynolds number. It should also be noted that the mass loading corresponding to the experimental measurements shown in the figure is 2%. Kulick *et al.* (1994) also measured particle velocity statistics at higher mass loading where the effect of particles on fluid turbulence becomes significant.

Thus, it is clear there are differences between the LES and experimental measurements of the copper velocities at $Re_\tau = 644$. Kulick *et al.* (1994) attributed the increase in near-wall copper velocity to the possibility that high-speed particles rebounding from the wall maintain a significant fraction of their streamwise momentum. The plateau in the copper velocity profile near the wall is consistent with notion of elastic collisions of high-speed particles contacting the wall and is also in agreement with recent examinations of particle deposition which have shown that particles are brought to the near wall region by events with normal velocity much larger than the local turbulence intensity (Brooke *et al.* (1994). Unlike the experimental measurements, however, the resulting copper mean velocity in the LES does not increase in the near wall region.

Comparison of rms particle velocity fluctuations from the LES to both DNS results and experimental measurements is shown in Figure 12 (for $Re_\tau = 180$) and Figure 13 (for $Re_\tau = 644$). As may be observed in Figure 12, there is in general good agreement between LES predictions and the DNS results of Rouson & Eaton (1994). It is clear from the figure that near the wall the streamwise fluctuation levels increase with increasing values of the Stokes number while the wall-normal and spanwise fluctuations are reduced. Comparison of the LES and DNS results also shows that the peak values in the LES profiles occur at slightly larger y^+ than in the DNS. It is further interesting to note that the streamwise rms velocities of the Lycopodium and glass beads from the LES calculations are smaller than the DNS values while the wall-normal and spanwise rms velocities in the LES are slightly greater than the corresponding values in the DNS.

Rms intensities from the channel at $Re_\tau = 644$ are shown in Figure 13. Velocity profiles for the Lycopodium particles are not available from the experiments; LES predictions are shown in Figure 13*a* for comparison and are consistent with the data at the lower Reynolds number, i.e., the Lycopodium fluctuations are nearly equal to the fluid values but lead in the streamwise direction while lagging in the wall-normal and spanwise directions. Experimental measurements of particle velocities are available for the 50μm glass beads and copper particles and it is evident in Figure 13*b* that there is good agreement between LES predictions and the measured streamwise intensities of the glass beads for $y^+ > 10$. The wall-normal fluctuations

in the experiment are greater than the LES values but the location of the peak in the wall-normal fluctuations is reasonably well predicted. The greatest discrepancy between LES and experimental measurements occurs for the copper particles. Figure 13c shows that the streamwise intensities in the experiment are larger than the LES predictions, and unlike the LES and DNS values at $Re_\tau = 180$, the streamwise intensities in the experiment peak at around $y^+ = 12$. Kulick *et al.* (1994) showed that the probability distribution function (pdf) of the streamwise copper velocity was bimodal at $y^+ = 12$, demonstrating that the streamwise copper intensities should not be interpreted as the width of a Gaussian velocity distribution. Pdfs of the copper velocities in the LES around $y^+ = 12$ were examined and not found to exhibit a similar bi-modal structure as in the experiment. Finally, comparison of the spanwise fluctuation levels for all the particles show a reduction with increasing Stokes number and greater similarity to the fluid for the smaller Stokes numbers.

It is difficult to speculate as to the precise cause of the differences between LES predictions and both DNS results and experimental measurements. Errors in the SGS model used in LES contribute to the differences as well as other factors such as the different particle sample sizes and the interpolation scheme used to obtain fluid velocities at particle positions in the computations. Another source of error in LES predictions of the particle velocity statistics is due to the neglect of particle transport by SGS velocities. In LES the smallest scales of motion are not resolved by the computational grid, only their effect on the large eddies is represented via the SGS model. Thus, only the large-scale velocity field is directly available in an LES computation for determining particle motion; for the results presented above the effect of subgrid-scale velocity fluctuations on particle transport were neglected. One measure of the error is the value of the particle relaxation time relative to the smallest resolved timescale in the LES, $T = \overline{\Delta}/(\overline{\Delta}|\overline{S}_1|) = 1/|\overline{S}_1|$. At $Re_\tau = 180$ the timescale T increases from about 0.011 near the wall to roughly 0.11 near the channel centerline while at $Re_\tau = 644$ increases from 0.002 to 0.08. Thus, some of the particle relaxation times considered in the LES are comparable to the smallest resolved timescale (see Tables 1 and 2).

The effect of the SGS velocity field on particle transport was investigated by adding SGS fluctuations to the fluid velocity used in the particle equation of motion (15), as outlined above. In the simulations SGS intensities were obtained from q^2 and specified to have the same relative magnitudes as the resolved-scale intensities. The component fluctuations u_i'' were then scaled by random numbers sampled from a Gaussian distribution and added to $\overline{u}_i$ at the particle location. The complete velocity, i.e., $\overline{u}_i + u_i''$, was subsequently used in (15) to determine the particle velocity. Figure 14 shows the wall-normal fluctuations for the 28μm Lycopodium particles at $Re_\tau = 644$ both with and without SGS velocity fluctuations included in (15). As is evident from the figure there is a negligible effect of the SGS fluid velocity on particle fluctuations. The relative difference is greatest near the wall where SGS fluctuations are large compared to the resolved components but the change in the wall-normal particle velocities due to addition of the SGS fluid velocity is less than 1%. Although not

shown here, the difference in particle fluctuations in the other directions is similar and there is essentially no effect on the mean streamwise particle velocity. Figure 14 demonstrates the strong filtering effect of particle inertia on the the fluid velocity spectrum. For particles with material densities large compared to the carrier flow the response of particles to the frequency spectrum of the turbulence can be shown to be proportional to $1/(\tau_p\omega)^2$ (ω is the frequency). Thus, for increasing values of the relaxation time and/or frequency the filtering of high frequency motions by particle inertia is significant, consistent with the results in Figure 14.

Both experimental measurements and numerical simulations have shown that inertial bias in particle trajectories results in a preferential concentration of particles in regions of low vorticity or high strain rate (see Eaton & Fessler 1994 for a general review). In wall-bounded shear flows it is reasonably well known that particle concentration fields near the wall are non-uniform with the largest number densities occurring in the low speed streaks (Pedinotti *et al.* 1992, Rouson & Eaton 1994). It is also important to point out, however, that recent investigations have shown that preferential concentration occurs throughout the channel (Fessler *et al.* 1994). Furthermore, Wang & Maxey (1993) have shown that preferential concentration obeys Kolmogorov scaling, i.e., particles with time constants and settling velocities close to the Kolmogorov scales will exhibit the largest effects of preferential concentration. Since the smallest scales of motion in LES are not resolved, it is of interest to examine the degree to which preferential concentration is reproduced in the present LES.

Structural Features

Shown in Figure 15*a* are streamwise velocity contours in an x-z plane at $y^+ = 3.6$ at $Re_\tau = 180$. As evident in the figure, the streaky structure of the near-wall region is represented in the LES. The instantaneous particle distribution in the same plane and at the same time is also shown in Figure 15. A streaky structure in the number density of the Lycopodium particles similar to that observed in the velocity field is apparent in Figure 15*b*. It is also clear from the figure that the number density is less well organized for the 50μm glass beads and the copper particle distribution in Figure 15*d* appears random. Similar behavior was also observed by Rouson & Eaton (1994) using DNS and demonstrates that at $Re_\tau = 180$ the LES does represent, at least qualitatively, preferential concentration of particles by turbulence. The streamwise velocity contours in an x-z plane at $y^+ = 4.8$ and $Re_\tau = 644$ are shown in Figure 16*a*. As can be seen from the figure, the streaky structure of the streamwise velocity is also evident at the higher Reynolds number. Number density distributions for the 28μm Lycopodium, 50μm glass beads, and 70μm copper particles are shown in Figures 16*b*, 16*c*, and 16*d*, respectively, and are similar to those obtained at the lower Reynolds number. Lycopodium particles again exhibit a structure somewhat similar to the velocity field and appear more organized than the glass beads and copper particles.

Fessler *et al.* (1994) have demonstrated that preferential concentration also occurs along the centerline of turbulent channel flow. In addition to the five types of particles examined in the experiments two sets of Lycopodium particles with smaller diameters were used in

the LES at $Re_\tau = 644$ to further examine the effect of response time on preferential concentration (see Table 2). Both visualizations and quantitative measures were obtained in the experiments and therefore provide a suitable benchmark for comparison to LES predictions.

The instantaneous particle distributions along the channel centerline from the LES calculation at $Re_\tau = 644$ are shown in Figure 17. Similar to the behavior observed by Fessler *et al.* (1994) the figure show that the copper particles are randomly distributed whereas the Lycopodium particles and glass beads exhibit varying degrees of preferential concentration. Of the three types of particles shown in Figure 17*a-c*, the preferential concentration of the 25μm glass beads appears more significant than for the Lycopodium particles, which is in turn stronger than for the 50μm glass beads. Thus, results in the figures again demonstrate that the LES reflects preferential concentration of particles by turbulence and exhibits the same qualitative features as in the experiments.

One approach to quantifying preferential concentration is through calculation of the pdf of the particle number density. For a random distribution of particles the pdf is Poisson distributed,

$$F_p(k) = \frac{e^{-\lambda}\lambda^k}{k!}\,, \tag{19}$$

where λ is the average number of particles per cell. Shown in Figure 18 are pdfs of the particle number density at $Re_\tau = 644$ together with the Poisson distribution. The pdf was calculated by subdividing the region $0.975 \leq y/\delta \leq 1.025$ into a network of cells of cross-sectional area 2.6mm^2 (in the x-z plane). The pdf of copper particles is very similar to the Poisson distribution whereas the other particles differ significantly from a random distribution; the greatest difference appearing to occur for the 25μm glass beads. Thus, consistent with Figure 17 as well as Fessler *et al.* (1994). Figure 18 shows that preferential concentration is not a monotonic function of the Stokes number.

Fessler *et al.* (1994) also defined as a measure of preferential concentration the deviation from a Poisson distribution,

$$D = \frac{\sigma - \sigma_p}{\lambda}\,, \tag{20}$$

where σ and σ_p are the standard deviations for the measured particle distribution and the Poisson distribution, respectively. For particles exhibiting preferential concentration some cells have large number densities whereas other cells substantially lower number densities relative to the mean, resulting in large positive values of D. Since number densities are obtained by defining a network of cells in an x-z plane, it is therefore important to consider the effect of the cell size when calculating D. For very small cell sizes, the dimension of a cell is smaller than the Kolmogorov lengthscale and the particle distribution will appear random, resulting in D being zero. For very large cells, regions of high and low particle number density will be contained within the same cell and the resulting value of D will also be close to zero. Between these two extremes there is a cell size where D is maximized (see Fessler *et al.* 1994 for further discussion).

As shown in Fessler *et al.* (1994) the cell size at which (20) is maximum is a function of

the particle type. Therefore, pdfs of the number density field along the channel centerline were calculated using several cell sizes. The maximum value from (20), D_{max}, in the LES is compared to Fessler *et al.* (1994) in Figure 19. Both the LES and the experiments indicate that D_{max} exhibits a peak and is largest for the 25μm glass beads. Wang & Maxey (1993) used DNS of isotropic turbulence and showed that preferential concentration of heavy particles obeys Kolmogorov scaling. Fessler *et al.* (1994) estimated the Kolmogorov timescale and found that the ratio of the response time for 25μm glass beads to the Kolmogorov timescale is 2.2. However, the Stokes number defined in terms of the Kolmogorov timescale for the 28μm Lycopodium is 0.74 and thus the results in Figure 19 seem to contradict Wang & Maxey (1993). Fessler *et al.* (1994) attributed a possible cause of the discrepancy to the wider range of lengthscales in the experiment as compared to DNS. In this regard it is interesting to note that while the LES is performed at the same Reynolds number as the experiment, the range of scales in the computation is smaller since the subgrid-scale motions are not resolved. Thus, it is unlikely that the 25μm glass beads exhibit slightly stronger effects of preferential concentration because of an extended range of scales. A more likely cause of the discrepancy, which is discussed by Fessler *et al.* (1994) is the difference between the cell size used for computation of the number density field relative to the Kolmogorov lengthscale in the experiment and DNS. Fessler *et al.* (1994) found that for smaller cell sizes the Lycopodium particles exhibited slightly larger values of D as compared to that for the 25μm glass beads. Similar behavior was observed when analyzing the LES results.

4.4.2 LES of particle-laden mixing layers

Simulation Overview

In this phase of Specific Aim 4, simulations of a particle-laden mixing layer were used to further validate the computational approach. The governing equations, numerical method, and schematic for the temporally evolving flow have been described earlier.

The initial condition for the velocity field is from a separate LES calculation of turbulent channel flow at Reynolds number based on friction velocity and channel half-width of 180 and described in the previous subsection. The Reynolds number based on the initial momentum thickness θ_0 and velocity difference ΔU is $Re = \Delta U \theta_0 / \nu = 710$. The momentum thickness is defined as

$$\theta = \frac{1}{(\Delta U)^2} \int_{-\infty}^{\infty} \left(\langle \overline{u} \rangle_{xz} + U \right) \left(U - \langle \overline{u} \rangle_{xz} \right) dy \ , \tag{21}$$

where $\langle \ \rangle_{xz}$ denotes an average in x-z planes and θ_0 is the initial value. The Reynolds number based on the free stream velocity and boundary layer thickness on one side of the layer is $Re_b = U\theta_b/\nu = Re/4 = 177$, where the boundary layer thickness is defined as

$$\theta_b = \int_0^{\infty} \frac{\langle \overline{u} \rangle_{xz}}{U} \left(1 - \frac{\langle \overline{u} \rangle_{xz}}{U} \right) dy \ . \tag{22}$$

The value of Re_b from the LES is smaller than the measured value of 200 in the high speed side of the experiment by Hishida *et al.* (1992) but larger than that in the low speed side of the

experiments. The size of the computational domain in the streamwise direction, $L_x = 116\theta_0$, and in the spanwise direction, $L_z = 39\theta_0$, are the same as the domain size in the channel flow. The domain size in the cross-stream direction was increased to $L_y = 233\theta_0$ in order to minimize any adverse effects of the cross-stream boundary condition on the evolution of the layer. The flow was resolved using $64 \times 65 \times 128$ grid points in the x, y, and z directions, respectively. While a uniform mesh was used in the streamwise and spanwise directions, a stretched grid was used in the cross-stream direction such that the grid spacing near the centerplane is smaller. For the temporally evolving layer periodic boundary conditions are appropriate for the streamwise and spanwise directions. No-stress boundary conditions were applied in the cross-stream direction, i.e., $\overline{u}_2 = \partial\overline{u}_1/\partial x_2 = 0$ where $\overline{u}_1$ and $\overline{u}_2$ are the streamwise and cross-stream velocity, respectively.

Properties of the dispersed phase were obtained by following the trajectories of 20,000 particles satisfying (15). The particles used in the simulations possess material characteristics identical to those in the experiments of Hishida *et al.* (1992): 42, 72, and 135μm diameter glass beads; the particle response time, which is defined as $\tau_p = \rho_p d^2/(18\rho_f \nu)$ is 0.014, 0.041 and 0.144s, respectively. For these diameters and sample sizes the dispersed phase volume fraction varies from 10^{-5} for the smaller particles to 10^{-4} for the 135μm beads. For volume fractions in this range particle collisions are relatively less important (e.g., Crowe *et al.* 1996). However, in the central part of the layer, where particles were injected in the experiment and initially seeded in the computations, local values of the volume fraction may be large enough such that collisions are significant. The reader is referred to recent the work of Sommerfeld (1995) and Laviéville *et al.* (1995) for additional discussion of particle collisions.

In the experiments of Hishida *et al.* (1992), particles were injected from a nozzle near the splitter plate. In the calculations particles are initially (randomly) distributed in x-z planes $-0.5D \leq y \leq 0.5D$, where $D = 0.57$mm is the nozzle diameter. The three groups of particles have the same initial distribution and same initial velocity. The initial particle velocities are designed to match those of the 135μm particles in the experiment (injection velocities for other particle sizes were not measured). LES predictions in the temporally evolving flow are compared to the spatially developing experimental results by first using the convection velocity in the experiment (8.5m/s) to transform from downstream evolution to time. LES predictions are then compared to the experimental results at equivalent times made dimensionless using the local momentum thickness and velocity difference ΔU.

Statistical Features - Fluid

Shown in Figure 20a is the evolution of the momentum thickness along with the DNS results of Rogers & Moser (1994) for their unforced case. For a self-similar mixing layer the momentum thickness should increase linearly in a temporally evolving flow (downstream location in a spatially evolving layer). It is evident that the momentum thickness increases linearly after $\tau \equiv t\Delta U/\theta_0 \approx 50$. The dimensionless layer growth rate

$$r = \frac{1}{\Delta U}\frac{d\theta}{dt} = \frac{d}{d\tau}(\theta/\theta_0) \ , \tag{23}$$

is about 0.017, which is slightly larger than the value of 0.014 from Rogers & Moser (1994). In a spatially developing mixing layer, the equivalent nondimensional growth rate is

$$r = \frac{U_c}{\Delta U}\frac{d\theta}{dX} , \tag{24}$$

where U_c is the convection velocity and X the downstream location. The range of r in the experiments quoted by Dimotakis (1991) is 0.014–0.022. Thus, the growth rate from the LES agrees very well with the experimental data. Figure 20a also shows that the momentum thickness increases by a factor of about 6 from $\tau = 0$ to $\tau = 330$, indicating that the Reynolds number based on the momentum thickness θ and the velocity difference ΔU increased from 710 to 4,460.

In the self-similar region the ratio of the vorticity thickness

$$\delta_\omega = \frac{\Delta U}{(\partial\langle\overline{u}_1\rangle_{xz}/\partial y)_{max}} , \tag{25}$$

to the momentum thickness in the LES is about 4.5, close to the value of 4.8 obtained by Rogers & Moser (1994). This ratio is 4.44 for an error function mean velocity profile and 4.0 for a hyperbolic tangent velocity profile. The Reynolds number based on vorticity thickness increased to over 20,000 in the LES, high enough such that the current simulations produce fully developed turbulence (see Rogers & Moser 1994 for further discussion). In comparison with experiments on particle-laden mixing layers this value is larger than the range of $Re_\omega \sim 1,000 - 4,500$ in Wen *et al.* (1992) and $Re_\theta \sim 2,700$ in Hishida *et al.* (1992) while it is about half of the value $Re_\theta \sim 9,700$ in Lazaro & Lasheras (1992a,b) and Kiger & Lasheras (1995).

The evolution of the dissipation rate of turbulent kinetic energy

$$\mathcal{E} = \int_{-\infty}^{\infty} \langle(\nu + \nu_T)|S|^2\rangle_{xz} dy , \tag{26}$$

is shown in Figure 20b, where the dissipation rate is normalized by ΔU^3, along with the results from Rogers & Moser (1994). Also shown in the figure is the molecular dissipation $\int_{-\infty}^{\infty} \nu\langle|S|^2\rangle_{xz} dy$ and SGS contribution $\int_{-\infty}^{\infty}\langle\nu_T|S|^2\rangle_{xz} dy$. It is interesting to note that the magnitude of the dissipation rate in LES is close to that of Rogers & Moser (1994) for $\tau > 50$. For a self-similar mixing layer, the total dissipation rate should be a constant. At large τ, the dissipation rates from both LES and DNS decrease, suggesting that self-similarity does not hold at later times. The self-similar region, as indicated by the region of constant dissipation, in the LES is roughly from $140 < \tau < 280$. It is also evident from Figure 20b that the SGS dissipation is significant compared to the molecular value in the self-similar region.

The mean velocity profiles at four times in the self-similar region are shown in Figure 21 along with those from Rogers & Moser (1994) and the experimental measurements of Bell & Mehta (1990). It is clear that the collapse of the scaled mean profile is excellent and in good agreement with both DNS results and experimental data. The resolved Reynolds

stresses $\langle u_i'' u_j'' \rangle$, where $u_i'' = \overline{u}_i - \langle \overline{u}_i \rangle_{xz}$, at the same times are compared with the DNS and experiments in Figure 22. The collapse of the scaled Reynolds stress is quite good and also agrees reasonably well with DNS and experiments.

Statistical Features - Particles

Shown in Figure 23 are profiles of the particle number density at four times in the calculation corresponding to downstream locations in the experiment ranging from $100 \leq X \leq 250$mm. It is evident that the peak values decrease with time, indicating lateral transport of particles from their initial location near the centerplane. Consistent with the experimental measurements of Hishida *et al.* (1992), the 42μm particles are transported further from the centerplane than the larger particles, as evidenced by the smaller centerline peak for the 42μm particles in the figure. The figure also shows that the particle number density field is statistically symmetric about the centerplane, which is different from the experimental measurements where the peak concentration for the small particles was displaced to the low-speed side. This discrepancy is due to the asymmetry in the velocity field in experiments and the symmetric initial conditions in the LES. Since the initial conditions of the particles are also symmetric about the origin, the unequal entrainment on the low and high speed sides in the experiment is not reproduced in the computations.

Figure 24 shows the comparison of the mean and rms fluctuating fluid velocities from the LES to the measurements of Hishida *et al.* (1992). LES predictions of the mean flow are in generally good agreement with the experiment. As can be seen in the figure, small differences exist between the LES predictions and experiments. The rms velocities from the calculation also agree reasonably well with the experimental data, though the LES predictions tend to be slightly larger than the measured values. The discrepancy between the LES and Hishida *et al.* (1992) in the mean and fluctuating fluid velocity is likely due to the different development in the experiments and calculations. It should also be pointed out that maximum rms velocities vary in experiments and, as discussed by Dimotakis & Brown (1976), mixing layers only slowly "forget" the details of their initial conditions. The differences in the statistical evolution of the fluid velocity field will in turn lead to discrepancies between LES predictions and experimental measurements of particle velocities.

The mean particle streamwise velocity profiles from the LES are compared with those from Hishida *et al.* (1992) in Figure 25. While the agreement of the mean velocity for the 42μm particles is reasonable, the mean velocities for the larger particles predicted in the LES are smaller than the measurements. As discussed in §2.3, downstream displacement in the experiments is transformed to temporal evolution using the convection velocity $U_c = 8.5$m/s. This transformation is suitable for particles with an average speed near the convection velocity. In the experiments the average injection velocity was about 10% of U_c (Hishida *et al.* 1992). Thus, larger particles with increasingly greater inertia will require a longer development in order to approach the layer convection velocity. Thus, particle displacement, X_p, in the experiment will be less than the corresponding downstream displacement, X, of the fluid. Therefore, a more accurate comparison of the particle velocities in the LES and

experiment can be obtained by considering the downstream evolution appropriate to each particle size, rather than the convection velocity of the fluid.

LES predictions of the rms particle velocity fluctuations and correlation $\langle v_1'' v_2'' \rangle$ are compared to the measurements from Hishida *et al.* (1992) in Figures 26–28 ($v_i'' = v_i - \langle v_i \rangle$ is the particle velocity fluctuation). LES predictions are in reasonable agreement with the experiment and better than can be obtained using Reynolds-averaged methods (e.g., see Sommerfeld 1992). In general, the velocity fluctuations decrease with increasing values of the diameter (or Stokes number), and the fluctuation levels in the streamwise direction are much larger than in the cross-stream direction. It should be noted that the comparisons shown in Figures 26–28 are approximate since the fluid convection velocity has been used for transformation of the spatially developing experimental results to the temporal frame rather than the particle-dependent locations. However, since the experimental measurements of the fluctuating velocities show a less significant dependence on downstream evolution than the mean, the difference between the two transformations is small.

Insight into the behavior of the statistics in Figures 26–28 can be gained through consideration of the transport equation for the particle kinetic stresses. As shown by Simonin *et al.* (1995), the transport equation for the fluctuating quantity $\langle v_i'' v_j'' \rangle$ can be obtained from the particle equation of motion (15)

$$\left[\frac{\partial}{\partial t} + V_m \frac{\partial}{\partial x_m} \right] \langle v_i'' v_j'' \rangle = P_{ij} + T_{ij} + \Pi_{ij} \,, \tag{27}$$

where the mean particle velocity $V_i = \langle v_i \rangle$. The first term on the right-hand side represents production via the mean gradient of the particle velocity

$$P_{ij} = -\langle v_i'' v_m'' \rangle \frac{\partial V_j}{\partial x_m} - \langle v_j'' v_m'' \rangle \frac{\partial V_i}{\partial x_m} \,, \tag{28}$$

while the second term represents transport by the particle velocity fluctuations

$$T_{ij} = -\frac{1}{\alpha} \frac{\partial}{\partial x_m} \left[\alpha \langle v_i'' v_j'' v_m'' \rangle \right] \,, \tag{29}$$

where α is the volume fraction of the dispersed phase. The last term represents the momentum transfer rate from the fluid turbulence and is expressed as

$$\Pi_{ij} = -\left\langle \frac{\rho_f}{\rho_p} \frac{3}{4} \frac{C_D}{d} |\mathbf{v} - \mathbf{u}| \left[(v_i'' - u_i'') v_j'' + (v_j'' - u_j'') v_i'' \right] \right\rangle \,. \tag{30}$$

Note that, strictly speaking, Π_{ij} should also appear in (3) to account for the effect of particles on the fluid momentum. However, in the present case in which particle volume fractions are small, there is negligible effect of the particles on the fluid. As also shown by Simonin *et al.* (1995), Π_{ij} can be approximated as

$$\Pi_{ij} \approx -\frac{1}{\tau_A} \left[2\langle v_i'' v_j'' \rangle - \langle u_i'' v_j'' \rangle - \langle u_j'' v_i'' \rangle \right] \,, \tag{31}$$

where the mean particle relaxation time

$$\tau_A = \frac{\rho_p}{\rho_f}\frac{4}{3}\frac{d}{C_{DA}}\frac{1}{\langle|\mathbf{v}-\mathbf{u}|\rangle}, \tag{32}$$

and C_{DA} is the drag coefficient evaluated at the average particle Reynolds number.

For the temporally evolving mixing layer, the production term is non-zero in the streamwise direction, i.e., $P_{11} = -2\langle v_1'' v_2''\rangle \partial V_1/\partial x_2 > 0$. Figure 25 shows that the cross-stream gradient of the mean particle velocity for the different diameters are similar, and Figure 28 shows that the particle kinetic shear stress decreases with increasing diameter. Consequently, production of streamwise fluctuations through interaction with the mean flow will also decrease with increasing diameter, which contributes to the decreasing streamwise velocity fluctuation level for smaller diameter particles. Moreover, the particle kinetic stress can also be produced by the momentum transfer from fluid turbulence through Π_{ij}. As shown clearly in (31) the momentum transfer term is inversely proportional to the mean particle relaxation time τ_A. Since the relaxation time is proportional to the square of the diameter, the magnitude of kinetic stress production through Π_{ij} will be expected to decrease with increases in diameter (for the same density ρ_p). However, whether Π_{11} is a source or sink for the streamwise fluctuations depends on the value of $\langle u_1'' v_1''\rangle$ relative to $\langle v_1'' v_1''\rangle$.

While the streamwise component of the kinetic stress extracts energy through interactions with the mean flow, there is no direct exchange of energy between the mean and cross-stream fluctuations, i.e., $P_{22} = 0$. Figures 26 and 27 show that the cross-stream fluctuations are smaller than the streamwise values. The lack of mean-gradient production in the cross-stream direction contributes to the difference in the levels of the component fluctuations. Fluctuation levels in the cross-stream direction are generated by the transport term T_{22} as well as through the transport from fluid turbulence through the drag, Π_{22}. With increasing τ_A, the momentum transfer term from fluid turbulence is reduced, which can in turn be expected to reduce the particle velocity fluctuations.

Overall, the agreement between the LES and experiments is reasonable. It is difficult to precisely capture the streamwise development of the layer in the experiment, i.e., the different initial conditions in the simulation and experiment will contribute to the discrepancies between LES predictions and measurements. In the LES, the layer evolves from the boundary layers on either side of a fully developed channel flow. The conditions of the splitter plate boundary layers in the experiment are not discussed in Hishida *et al.* (1992). The velocity profile slightly downstream of the splitter tip in the experiment exhibits a slight wake component, an aspect also not replicated in the calculations. Hishida *et al.'s* (1992) measurements indicate that after the momentum thickness has increased by about a factor of seven the layer is relatively independent of the conditions near the splitter tip (i.e., at the station $X = 100$mm in the experiment). The LES attains a nearly self-similar behavior after the momentum thickness has increased by less than a factor of three. All of these factors contribute to differences observed between LES predictions and experimental measurements. Slight differences in the initial particle velocities between simulation and experiment will also

lead to a different evolution of the statistics.

Another source of error in LES predictions is due to the neglect of particle transport by SGS velocity fluctuations. In the calculations of the Eulerian velocity field, the smallest scales of motion are not resolved by the computational grid, only their effect on the large eddies is represented via the SGS model. Thus, only the large-scale velocity field is directly available for determining particle motion; for the results presented above the effect of subgrid-scale velocity fluctuations on particle transport was neglected. To investigate the effect of the SGS velocity fluctuations on particle transport another series of calculations were performed in which SGS fluctuations were added to the fluid velocity used in the particle equation of motion (15). The fluid velocity in (15) was the resolved component, $\overline{u}_i$, directly available in the LES, plus a subgrid contribution, u_i'''. The magnitude of the SGS fluctuation u_i''' was determined from the SGS turbulent kinetic energy, q^2. The SGS kinetic energy is not directly available and must be estimated using a model. Similar to Moin *et al.* (1991), the SGS energy is parameterized using the closure postulated by Yoshizawa (1986),

$$q^2 = \overline{u_i u_i} - \overline{u}_i \overline{u}_i = 2 C_q \overline{\Delta}^2 |\overline{S}_1|^2 \ . \tag{33}$$

The model coefficient C_q can be determined dynamically using the resolved velocity field in a similar manner as the coefficient C in the eddy viscosity by assuming the subtest energy has similar parameterization as (33), i.e.,

$$\widehat{\overline{u_i u_i}} - \widehat{\overline{u}_i}\,\widehat{\overline{u}_i} = 2 C_q \hat{\overline{\Delta}}^2 |\hat{\overline{S}}|^2 \ . \tag{34}$$

Test filtering (33) and then subtracting from (34) yields

$$C_q = \frac{\left\langle \widehat{\overline{u_i u_i}} - \widehat{\overline{u}_i}\,\widehat{\overline{u}_i} \right\rangle_{xz}}{\left\langle 2\overline{\Delta}^2 \left(\alpha^2 |\hat{\overline{S}}|^2 - |\widehat{\overline{S}}|^2 \right) \right\rangle_{xz}} \ . \tag{35}$$

Note that both denominator and numerator have been averaged over x-z planes. Shown in Figure 29 is the cross-stream profile of the SGS turbulent kinetic energy q^2 along with that of the resolved velocity $e^2 = u_1'^2 + u_2'^2 + u_3'^2$. The SGS energy q^2 along the centerplane is about 8% of the resolved-scale energy e^2, slightly larger than that in the turbulent channel flow.

In the calculation, the SGS component fluctuations were obtained using q and specified to have the same relative magnitude as the resolved-scale intensities. The component fluctuations u_i''' were then scaled by random numbers sampled from a Gaussian distribution and added to $\overline{u}_i$ at the particle location. The complete velocity, i.e., $\overline{u}_i + u_i'''$, was subsequently used in (15) to determine the particle velocity. Figure 30 shows the comparison of the rms streamwise particle velocities with and without the contribution from the SGS model. There is a relatively small effect of the SGS velocity on the particle fluctuation levels, the effect being more significant for the smaller particles which possess a smaller relaxation time. The results in Figure 30 illustrate the strong filtering of high frequency motions by particles with

densities substantially larger than the carrier fluid. Although not shown here, the difference in other second order statistics is similar to that shown in the figure and there is essentially no effect of SGS velocities on the mean particle velocity.

Structural Features

Both experiments and computations have shown that particle dispersion in free shear flows is largest for particles with relaxation times comparable to the timescale of the large-scale coherent motions typically observed in these flows. The dispersion of particles with Stokes numbers around unity may be larger than that of fluid elements since they can be flung from the core region of large-scale vortices (see e.g., Crowe *et al.* 1996). However, as mentioned previously, the Stokes number scaling in a turbulent mixing layer evolving from fully developing turbulent initial conditions may not be similar to that in flows with well-defined initial conditions. A series of calculations were performed for glass beads with diameters ranging from 1.5μm to 135μm. For each diameter, the trajectories of 20,000 particles were tracked in the simulations. Particles were initially located along the centerplane of the layer $y = 0$ and their velocity was initially zero. The particles are characterized by their Stokes number $St = \tau_p/\tau_f$, where τ_f is the large eddy time scale (see Crowe *et al.* 1996). The flow time scale is defined using a length scale and the velocity difference between the upper and lower streams.

Figure 31 shows the particle mean-square dispersion in the cross-stream direction,

$$\langle Y^2 \rangle(t) = \left\langle (y(t) - y_0)^2 \right\rangle = \left\langle y^2(t) \right\rangle \ , \tag{36}$$

where $y_0 = 0$ is the initial location and $\langle\ \rangle$ denotes an ensemble average over all particles with the same Stokes number. It is clear that the smallest particles (1.5μm) follow the flow while the dispersion of larger particles can lead or lag the fluid. At earlier times $\langle Y^2 \rangle$ is largest for fluid elements whereas particles with larger Stokes number exhibit the greatest mean-square dispersion at later times.

In order to quantify the dispersion of finite-inertia particles relative to fluid elements, the following four quantities were calculated: (1) the ratio of $\langle Y^2 \rangle$ for particles to that of fluid elements, $\langle Y^2 \rangle_p / \langle Y^2 \rangle_f$, where $\langle\ \rangle_p$ denotes an average over finite-inertia particles with the same St and $\langle\ \rangle_f$ an average over fluid elements; (2) the ratio of eddy diffusivity $\epsilon = d\langle Y^2 \rangle / dt/2$ of particles to fluid elements, ϵ_p/ϵ_f; (3) the ratio of maximum displacement before a specific time of particles to fluid elements, $\langle |Y|_{max} \rangle_p / \langle |Y|_{max} \rangle_f$; (4) the ratio of particle displacement at a specific time (averaged over all particles) to fluid elements, $\langle |Y| \rangle_p / \langle |Y| \rangle_f$. The quantity $\langle Y^2 \rangle_p / \langle Y^2 \rangle_f$ is the most common measure and has been used by several investigators in the study of particle dispersion in free shear flows (e.g., see Crowe *et al.* 1996 and references therein). The ratio of eddy diffusivities was used by Hishida *et al.* (1992) but it is important to note the measure used in their work (and in the present simulations) is strictly applicable to homogeneous turbulence. The quantity $\langle |Y|_{max} \rangle_p / \langle |Y|_{max} \rangle_f$ was used by Chein & Chung (1987) in simulations of a mixing layer in which one of their interests was on the effect of vortex pairing on dispersion. For flows in which pairing strongly influences the dispersion

process, $\langle|Y|_{max}\rangle_p/\langle|Y|_{max}\rangle_f$ is a relevant measure since it reflects the history of particle motion and the fact that dispersion can exhibit a wavy trend in response to the pairing process (Chein & Chung 1987). The fourth, $\langle|Y|\rangle_p/\langle|Y|\rangle_f$, depends on the particle position at a specific time, rather than on its history as does $\langle|Y|_{max}\rangle_p/\langle|Y|_{max}\rangle_f$. It should also be noted that other measures of dispersion can be obtained from profiles of the particle concentration but require a larger sample size than considered in this study.

Figure 32 shows the evolution of the four measures of dispersion as a function of the Stokes number defined using the initial vorticity thickness $St_0 = \tau_p/\delta_{\omega 0}/\Delta U$. At early times, the ratios shown in the figure are smaller than unity and their values decrease for larger St_0 due to increasing particle inertia. For increasing time (e.g., $\tau = 91$ in the figure) there is a peak, larger than unity, around $St_0 = 10$, indicating particle dispersion for this Stokes number is larger than those for both smaller and larger St_0. As time increases further the peak moves to larger Stokes numbers. Similar behavior has been observed in two-dimensional mixing layers evolving from an initial condition in which disturbances were superimposed on the initial profile. The fact that the Stokes number corresponding to maximum dispersion increases with time is also consistent with the mean-square dispersion shown in Figure 31, where $\langle Y^2\rangle$ is largest for the larger particles at longer evolution times.

Because of the time-dependent nature observed in quantities measuring dispersion such as those shown in Figure 32, it is perhaps more appropriate to define an effective Stokes number which reflects the time-dependent evolution of the flow. A time-dependent Stokes number can be defined using a local lengthscale; in particular, the local vorticity thickness, resulting in $St = \tau_p/\delta_\omega/\Delta U$. The same ratios from Figure 32 have been re-plotted in Figure 33 as a function of the time-dependent St. It is interesting to note the relatively good collapse of the curves, with the exception of the values at the earliest time $\tau = 108$. Furthermore, the maximum values occur near $St = 1$ at all times, consistent with the usual notion that dispersion is maximized for Stokes numbers near unity. For smaller St the particles behave similarly to fluid elements and have nearly identical dispersion while the dispersion of particles with larger St is much smaller than the fluid. More importantly, the results in Figure 33 show that to obtain maximum dispersion for $St = 1$, the appropriate length scale is the vorticity thickness. It is interesting to note that definition of the Stokes number using the vorticity thickness is approximately the same as defining St using the dominant frequency of the layer, as suggested by Aggarwal (1994). It can be shown, for example, that if the mixing layer evolves self-similarly from a well-defined mean velocity profile (e.g., hyperbolic-tangent), the ratio between St defined using the fundamental frequency of the time-dependent mean velocity and that defined using the local vorticity thickness is near unity (≈ 1.125). Thus, LES results indicate that the peak in dispersion for $St \approx 1$ is linked to the dominant frequency of the layer and that the vorticity thickness is the appropriate lengthscale for defining the Stokes number.

It should also be noted that since the lengthscales in a self-similar mixing layer grow linearly in time, other definitions of the Stokes number will yield results similar to Figure 33

with appropriate shifts in the horizontal axis. For example, defining the Stokes numbers using the time-dependent momentum thickness would result in maximums in the ratio of the mean-square dispersion occurring around a Stokes number of 4.5, which is the ratio of the vorticity thickness to the momentum thickness in the LES.

4.5 Conclusions

A methodology based on large eddy simulation was developed for prediction of particulate transport in turbulent flows. The focus was on model development and a systematic validation through comparison to experimental measurements in well-defined test problems. It is important and necessary to demonstrate that a computational approach being advocated for application to complex situations such as those encountered in ventilation systems first yield accurate predictions of "building block" flows. Any model which has not been first applied to well-defined test problems cannot be trusted to yield, for example, accurate descriptions of worker exposure in industrial ventilation settings.

The technique developed in this work was validated in a range of flows possessing complex physics (e.g., free shear flows vs. boundary layers). Overall, model predictions are in good agreement with experimental measurements and results from direct numerical simulations. To our knowledge, there is no other model capable of yielding comparable accuracy in prediction of the statistical and structural properties of particulate transport as obtained in this research.

The fact that LES provides an accurate description of statistical and structural features of particle transport implies that this technique may now be extended to a far wider range of industrial problems than have previously considered. The goal of future applications of LES should be to further advance the technique and, ultimately, provide a useful design tool for health professionals. Future applications should bring into focus the entire computational approach, i.e., resolution requirements, grid sizes, performance of the numerical method, evaluation of the turbulence model, etc. Given the successful completion of this project, two areas in which LES would be a useful tool for design and analysis are prediction of contaminant transport around a worker near a local exhaust device and simulation of transport in confined spaces. Poorly ventilated spaces have adverse effects on occupant health and comfort, resulting in significant costs for remediation. Current models fail to represent the complicated physics governing transport in these two areas and techniques based on LES may be the only viable approach to developing a *predictive* model.

5 Publications

Papers in Archival Journals

1. "On extension of the fractional step method to general curvilinear coordinate systems", X. Wu, K.D. Squires & Q. Wang, *Numerical Heat Transfer, Part B: Fundamentals*, **27**(2), pp. 175-194, 1995.

2. "Lagrangian statistics in turbulent channel flow", Q. Wang, K.D. Squires & X. Wu, *Atmospheric Environment*, **29**(18), pp. 2417-2427, 1995.

3. "Large eddy simulation of particle deposition in a vertical turbulent channel flow", Q. Wang & K.D. Squires, *Intnl. Journal of Multiphase Flow*, **22**(4), pp. 667-683, 1996.

4. "Large eddy simulation of particle laden turbulent channel flow", Q. Wang & K.D. Squires, *Physics of Fluids*, **8**(5), pp. 1207-1223, 1996.

5. "On the role of the lift force in turbulence simulations of particle deposition", Q. Wang, K.D. Squires, M. Chen & J.B. McLaughlin, *Intnl. Journal of Multiphase Flow*, **23**(4), pp. 749-763, 1997.

6. "Transport of heavy particles in a three-dimensional mixing layer", Q. Wang & K.D. Squires, accepted for publication in *J. Fluids Engineering*, 1997.

Invited Papers

1. "On the large eddy simulation of particle-laden turbulence" (invited paper), K.D. Squires & Q. Wang, *Proceedings of the 8^{th} Workshop on Two Phase Flow Predictions*, edited by M. Sommerfeld, 1996.

Refereed Conference Proceedings

1. "On the prediction of particle deposition in turbulent channel flow using large eddy simulation", Q. Wang & K.D. Squires, *Gas-Particle Flows*, edited by D.E. Stock, M.W. Reeks, Y. Tsuji, E.E. Michaelides, and M. Gautam, ASME-FED **228**, pp. 33-38, 1995.

2. "Particle transport in a nonuniformly seeded mixing layer", Q. Wang & K.D. Squires, *AIAA paper 96-0683*, 1996.

3. "Large eddy simulation of particle dispersion in a three-dimensional turbulent mixing layer", Q. Wang & K.D. Squires, *Numerical Methods for Multiphase Flow*, edited by C.T. Crowe, Y. Tsuji, A. Prosperetti, M. Sommerfeld, and R. Johnson, ASME-FED **236**, pp. 33-40, 1996.

4. "Comparison between two-fluid model predictions and large eddy simulation results in a vertical gas-solid turbulent channel flow", O. Simonin, Q. Wang & K.D. Squires, in *Proc. of the 1997 ASME Fluids Engineering Division Summer Meeting - Symposium on Gas-Particle Flows*, paper FEDSM97-3625, D. Stock, editor, 1997.

5. "Large eddy simulation of turbulent gas-solid flows in a vertical channel and modelling of particle velocity correlations", Q. Wang, K.D. Squires & O. Simonin, to appear in Proceedings of the Eleventh Symposium on Turbulent Shear Flows.

Conference Proceedings

1. "On the large eddy simulation of particle-laden channel flow", Q. Wang & K.D. Squires, *Sixth International Symposium on Computational Fluid Dynamics - A Collection of Technical Papers*, volume III, pp. 1363-1367, 1995.

Abstracts

1. "Lagrangian statistics obtained from large eddy simulations of turbulent channel flow", Q. Wang & K.D. Squires, *Bulletin of the American Physical Society*, **39**(9), p. 1845, 1994.

2. "On the subgrid-scale modeling of particle-laden turbulence", K.D. Squires, M. Boivin & O. Simonin, presented at the Twelfth U.S. National Congress of Applied Mechanics, University of Washington, Seattle, Washington, June 27-July 1, 1994.

3. "Large eddy simulation of particle dispersion in a 3D mixing layer", Q. Wang & K.D. Squires, *Bulletin of the American Physical Society*, **40**(12), p. 2018, 1995.

4. "On the evaluation of two-fluid models in particle-laden channel flow", Q. Wang, K.D. Squires & O. Simonin, *Bulletin of the American Physical Society*, **41**(9), p. 1784, 1996.

5. "On the particle kinetic stress budget and evaluation of second-order models in turbulent shear flows", Q. Wang & K.D. Squires, in Proceedings of the 1997 Joint ASME/ASCE/SES Summer meeting, 1997.

5.1 Planned Publications

1. "On the effect of nonuniform seeding on particle dispersion in two-dimensional mixing layers", Q. Wang, K.D. Squires & L.-P. Wang, submitted to *Physics of Fluids.*

2. "Direct numerical simulation of turbulence modulation by particles in isotropic turbulence", M. Boivin, O. Simonin & K.D. Squires, submitted to *J. Fluid Mech.*

3. "Large eddy simulation of turbulent gas-solid flows in a vertical channel and evaluation of second-order models", Q. Wang, K.D. Squires & O. Simonin, in prep.

4. "Large eddy simulation of particle-laden isotropic turbulence with two-way coupling", M. Boivin, O. Simonin & K.D. Squires, in prep.

References

[1] Aggarwal, S.K., 1994, "Relationship between stokes number and intrinsic frequencies in particle-laden flows," *AIAA J.*, **32**, pp. 1323-1325.

[2] Anastas, M.Y. & Hughes, R.T., 1989, "Finite difference methods for computation of flow into local exhaust hoods", *Am. Ind. Hyg. Assoc. J.*, **50**(10), pp. 526-534.

[3] Anastas, M.Y., 1991, "Computation of the initially unknown boundaries of flow fields generated by local exhaust hoods", *Am. Ind. Hyg. Assoc. J.*, **52**(9), pp. 379-386.

[4] Baturin, V.V., 1972, *Fundamentals of Industrial Ventilation.*, third edition, Pergamon Press, New York.

[5] Bell, J.H. & Mehta, R.D., 1990, "Development of a two-stream mixing layer from tripped and untripped boundary layers," *AIAA J.*, **8**, pp. 2034-2042.

[6] Breysse, P.N. & Swift, D.L., 1980, "Deposition of Large Particles in the Human Nasal Passage", presented at the American Industrial Hygiene conference, Houston, Texas, May 18-23.

[7] Brooke, J.W., Hanratty, T.J. & McLaughlin, J.B., 1994, "Free-flight mixing and deposition of aerosols" *Phys. Fluids*, **6**, p. 3404.

[8] Chein, R. & Chung, J.N., 1987, "Effects of vortex pairing on particle dispersion in turbulent shear flows," *Int. J. Multiphase Flow*, **13**, pp. 785-802.

[9] Conroy, L.M., Ellenbecker, M.J. & Flynn, M.R., 1988, "Prediction and measurement of velocity into flanged slot hoods", *Am. Ind. Hyg. Assoc. J.*, **49**, pp. 226-234.

[10] Crowe, C.T., Troutt, T.R. & Chung, J.N., 1996, "Numerical models for two-phase turbulent flows," *Ann. Rev. Fluid Mech.*, **28**, pp. 11-43.

[11] Dalla Valle, J.M. & Hatch, T., 1932, "Studies in the design of local exhaust hoods", *Trans. A.S.M.E.*, **54**, pp. 31-37.

[12] Dalla Valle, J.M., 1952, *Exhaust Hoods*, second edition, The Industrial Press, New York.

[13] Dimotakis, P.E., 1991, "Turbulent free shear layer mixing and combustion," in *High-speed-Flight Propulsion Systems*, in Progress in Astronautics and Aeronautics, edited by Murthy, S.N.B. and Curran, E.T., pp. 265-340.

[14] Dimotakis, P.E. & Brown, G.L., 1976, "The mixing layer at high Reynolds number: large-structure dynamics and entrainment," *J. Fluid Mech.*, **78**, pp. 535-560.

[15] Doull, J., Klaassen, C.D. & Amdur (editors), 1980, *Casarett and Doull's Toxicology: The Basic Science of Poisons.* Second Edition, Macmillan Publishing Co., New York.

[16] Eaton, J.K. & Fessler, J.R., 1994, "Preferential concentration of particles by turbulence," *Int. J. Multiphase Flow*, **20**, p. 169.

[17] Fessler, J.R., Kulick, J.D. & Eaton, J.K., 1994, "Preferential concentration of heavy particles in a turbulent channel flow," *Phys. Fluids*, **6**, p. 3742.

[18] Flynn, M.R. & Ellenbecker, J.M., 1985, "The potential flow solution for air flow into a flanged circular hood", *Am. Ind. Hyg. Assoc. J.*, **46**(6), pp. 318-322.

[19] Flynn, M.R. & Ellenbecker, J.M., 1987, "Empirical validation of theoretical velocity fields into flanged circular hoods", *Am. Ind. Hyg. Assoc. J.*, **48**, pp. 380-389.

[20] Flynn, M.R. & Miller, C.T., 1989, "The boundary integral equation method (BIEM) for modeling local exhaust hood flow fields", *Am. Ind. Hyg. Assoc. J.*, **50**(5), pp. 281-288.

[21] Flynn, M.R. & Miller, C.T., 1991, "Discrete vortex methods for the simulation of boundary layer separation effects on worker exposure", *Ann. occup. Hyg.* **35**(1), pp. 35-50.

[22] Flynn, M.R. & Ljungqvist, B., 1995, A review of wake effects on worker exposure. *Ann. occup. Hyg.* **39**(2), pp. 211-221.

[23] Garrison, R.P. & Wang, Y., 1987, "Finite element applications for velocity characteristics of local exhaust inlets", *Am. Ind. Hyg. Assoc. J.*, **48**(12), pp. 983-988.

[24] Garrison, R.P. & Park, C., 1989, "Evaluation of models for local exhaust velocity characteristics–part one: velocity contours for freestanding and bounded inlets", *Am. Ind. Hyg. Assoc. J.*, **50**(4), pp. 196-203.

[25] Germano, M., Piomelli, U., Moin, P. and W.H. Cabot, 1991, "A dynamic subgrid-scale eddy viscosity model", *Phys. Fluids*, **3** (7), p. 1760.

[26] Germano, M., 1992, "Turbulence: the filtering approach", *J. Fluid Mech.*, **238**, p. 325.

[27] Ghosal, S., Lund, T.S., Moin, P. & Akselvoll, K., 1995, "A dynamic localization model for large-eddy simulation of turbulent flows", *J. Fluid Mech.*, **286**, pp. 229-255.

[28] Hinds, W.C., 1982, *Aerosol Technology.* John Wiley & Sons, New York, pp. 69-100.

[29] Hishida, K., Ando, A. & Maeda, M., 1992, "Experiments on particle dispersion in a turbulent mixing layer", *Int. J. Multiphase Flow*, **18**(2), pp. 181-194.

[30] Kiger, K.T. & Lasheras, J.C., 1995, "The effect of vortex pairing on particle dispersion and kinetic energy transfer in a two-phase turbulent shear layer," *J. Fluid Mech.*, **302**, pp. 149-178.

[31] Kim, J. & Moin, P., 1985, "Application of a fractional-step method to incompressible Navier-Stokes equations", *J. Comp. Physics* **59**, pp. 308-323.

[32] Kim, J., Moin, P. & Moser R.D., 1987, "Turbulence statistics in fully developed channel flow at low Reynolds number", *J. Fluid Mech.*, **177**, pp. 133-166.

[33] Kobayashi, H., Masutani, S.M., Azuhata, S. & Arashi, N., 1988, "Dispersed phase transport in a plane mixing layer", in *Transport Phenomena in Turbulent Flows,* Hirata and Kasagi, eds., Hemisphere, pp. 433-446.

[34] Kulick, J.D., Fessler, J.R. & Eaton, J.K., 1994, "Particle response and turbulence modification in fully turbulent channel flow," *J. Fluid Mech.*, **277**, p. 109.

[35] Laviévill, J., Deutsch, E. and Simonin, O., 1995, "Large eddy simulation of interactions between colliding particles and a homogeneous isotropic turbulence field," in *Gas-Particle Flows*, FED-Vol. 228, pp. 347-357.

[36] Lazaro, B.J. & Lasheras, J.C., 1992a, "Particle dispersion in the developing free shear layer. Part 1. Unforced flow", *J. Fluid Mech.*, **235**, pp. 143-178.

[37] Lazaro, B.J. & Lasheras, J.C., 1992b, "Particle dispersion in the developing free shear layer. Part 2. Forced flow", *J. Fluid Mech.*, **235**, pp. 179-221.

[38] Lilly, D.K., 1992, "A proposed modification of the Germano subgrid-scale closure method", *Phys. Fluids*, 4, p. 633.

[39] Meneveau, C., Lund, T.S. & Cabot, W.H., 1996, "A Lagrangian dynamic subgrid-scale model of turbulence", *J. Fluid Mech.*, **319**, pp. 353-385.

[40] Moin, P., Squires, K.D., Cabot, W.H. & Lee, S., 1991, "A dynamic subgrid-scale model for compressible turbulence and scalar transport", *Phys. Fluids*, **3**, pp. 2746-2757.

[41] Moss, O., Kanapilly, G.M., 1980, "Dissolution of Inhaled Aerosols", in *Generation of Aerosols and Facilities for Exposure Experiments.* K. Willeke, ed., Ann Arbor Science, Michigan, pp. 105-124.

[42] Pedinotti, S., Mariotti, G. & Banerjee, S., 1992, "Direct numerical simulation of particle behaviour in the wall region of turbulent flows in horizontal channels," *Int. J. Multiphase Flow*, **18**, p. 927.

[43] Phalen, R.F., Hinds, W.C., John, W., Lioy, P.J., Lippman, M., McCawley M.A., Rabbe, O.G., Soderholm, S.C. & Stuart, B.O., 1986, "Rationale and Recommendations for Particle Size-Selective Sampling in the Workplace", *J. Appl. Ind. Hyg.*, **1**(3), p. 14.

[44] Rodi, W., 1980, *Turbulence models and their applications in Hydraulics.* International Associate for Hydraulic Research, Delft, The Netherlands.

[45] Rogers, M.M. & Moser, R.D., 1994, "Direct simulation of a self-similar turbulent mixing layer," *Phys. Fluids*, **6** (2), pp. 903-923.

[46] Rouson, D.W.I. & Eaton, J.K., 1994, "Direct numerical simulation of particles interacting with a turbulent channel flow," *Proceedings of the 7th Workshop on Two-Phase Flow Predictions*, M. Sommerfeld, editor, Erlangen, Germany.

[47] Schumann, U., 1991, "Subgrid length-scales for large-eddy simulation of stratified turbulence," *Theor. Comput. Fluid Dynamics* **2**, p. 279.

[48] Silverman, L., 1942a, "Centerline velocity characteristics of round hoods under suction", *J. Ind. Hyg. Toxicol.*, **24**, pp. 259-266.

[49] Silverman, L., 1942b, "Centerline velocity characteristics of narrow exhaust slots", *J. Ind. Hyg. Toxicol.*, **24**, pp. 267-276.

[50] Simonin, O., Deutsch, E. & Boivin, M., 1995, "Large eddy simulation and second-moment closure model of particle fluctuating motion in two-phase turbulent shear flows," in *Turbulent Shear Flow 9*, F. Durst, N. Kasagi, B.E. Launder, F.W. Schmidt, J.H. Whitelaw, editors, Springer-Verlag (Heidelberg), pp. 85-115.

[51] Smagorinsky, J., 1963, "General circulation experiments with the primitive equations. I. The basic experiment", *Mon. Weather Rev.*, **91**, pp. 99-164.

[52] Sommerfeld, M., 1992, *Sixth workshop on two-phase flow predictions*, Erlangen, Germany.

[53] Sommerfeld, M., 1995, "The importance of inter-particle collisions in horizontal gas-solid channel flows," in *Gas-Particle Flows*, FED-Vol. 228, pp. 335-345.

[54] Spalart, P.R., 1986, "Direct simulation of a turbulent boundary layer up to $Re_\theta = 1410$", *NASA Tech. Memo.* 89407.

[55] Squires, K.D. & Eaton, J.K., 1990, "Particle response and turbulence modification in isotropic turbulence", *Phys. Fluid A*, **2**, pp. 1191-1203.

[56] Squires, K.D. & Eaton, J.K., 1991a, "Preferential concentration of particles by turbulence", *Phys. Fluid A*, **3** (5, part 2), pp. 1169-1178.

[57] Squires, K.D. & Eaton, J.K., 1991b, "Measurements of particle dispersion obtained from direct numerical simulations of isotropic turbulence", *J. Fluid Mech.*, **226**, pp. 1-35.

[58] Tennekes, H. & Lumley, J.L., 1972, *A first course in turbulence*, The MIT Press, Cambridge.

[59] Wen, F., Kamalu, N., Chung, J.N., Crowe, C.T. & Troutt, T.R., 1992, "Particle dispersion by vortex structures in plane mixing layers," *J. Fluid Eng.*, **114**, pp. 657-666.

[60] Williams, G.P., 1969, "Numerical integration of the three-dimensional Navier-Stokes equations for incompressible flow", *J. Fluid Mech.*, **37**, pp. 727-750.

[61] Wang, L.-P. & Maxey, M.R., 1993, "Settling velocity and concentration distribution of heavy particles in homogeneous isotropic turbulence", *J. Fluid Mech.*, **256**, p. 27.

[62] Wu, X., Squires, K.D. & Wang, Q., 1995, "On extension of the fractional step method to general curvilinear coordinate systems", *Num. Heat Trans., Part B: Fundamentals*, **27**(2), pp. 175-194.

[63] Wu, X. & Squires, K.D., 1997, "Numerical investigation of the turbulent flow over a bump", submitted to *J. Fluid Mech.*.

[64] Yoshizawa, A., 1986, "Statistical theory for compressible turbulent shear flows, with application to subgrid modeling", *Phys. Fluid A*, **29**, pp. 2152-2164.

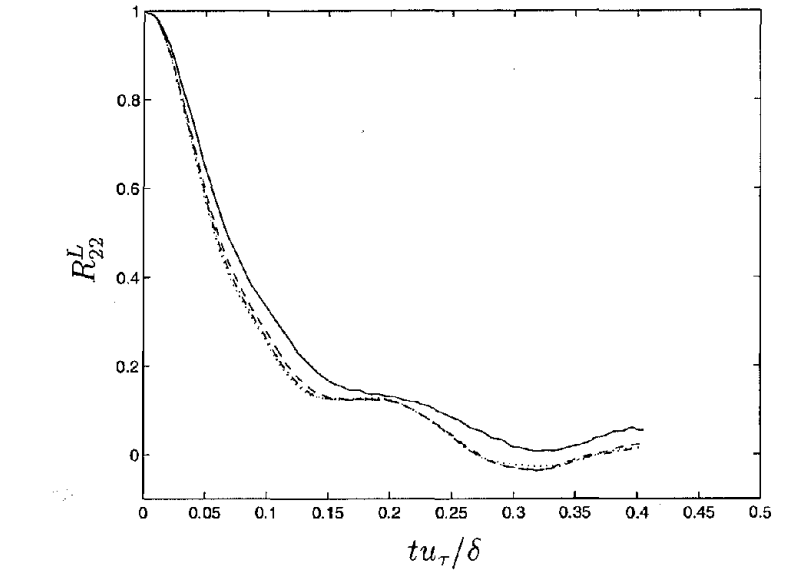

(a)

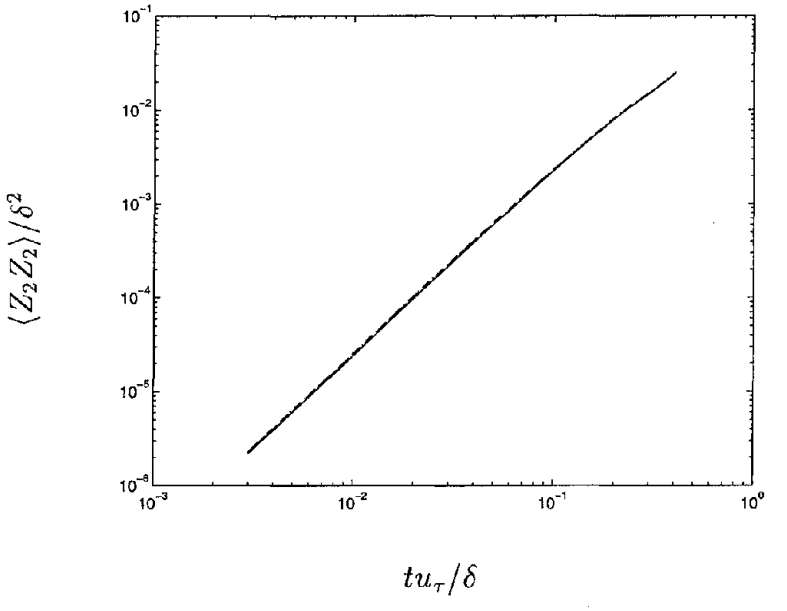

(b)

Figure 1: Effect of interpolation scheme on Lagrangian statistics. (a) Surface-normal component of Lagrangian velocity autocorrelation; (b) Surface-normal component of particle mean-square dispersion. —— linear interpolation; ---- 4th-order Lagrange Polynomials; —·— 6th-order Lagrange Polynomials; ····· cubic splines. The results in the figure show the largest errors incurred using linear interpolation and that the velocity correlation and mean-square dispersion are accurately resolved using fourth-order accurate Lagrange polynomials.

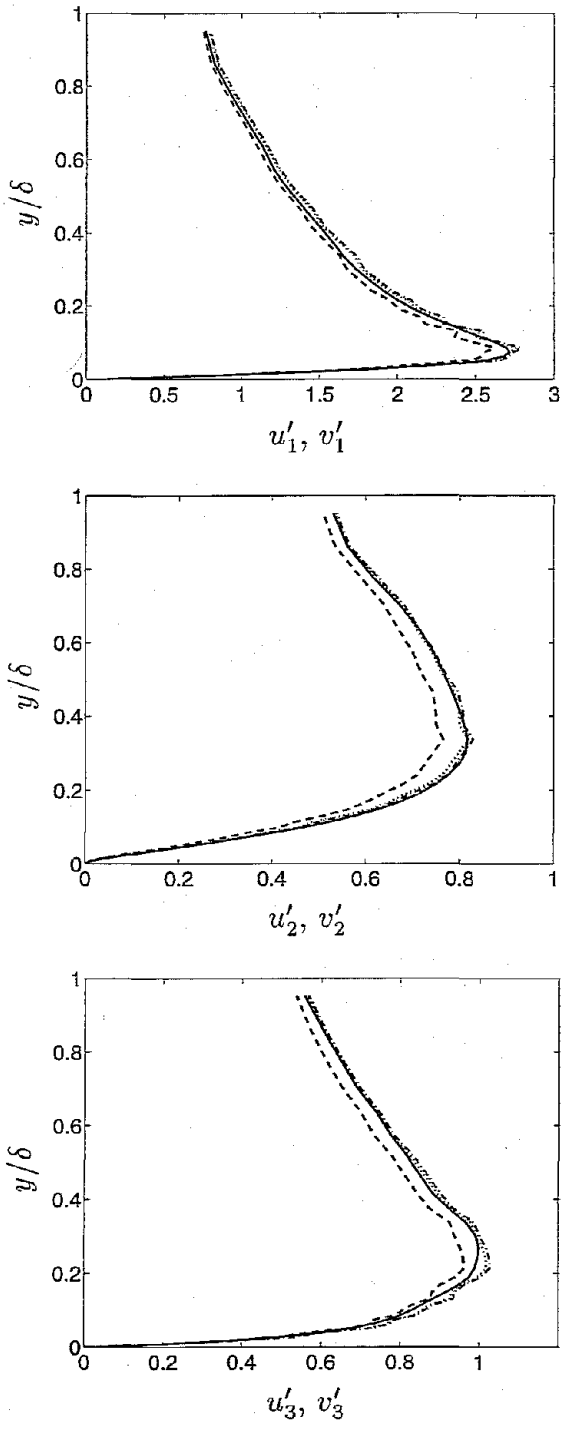

Figure 2: Effect of interpolation scheme on the fluctuating velocity in turbulent channel flow. —— Eulerian (reference value); ---- linear interpolation; ····· 4th-order Lagrange polynomials. The profiles from the Eulerian calculation (u_1', u_2', u_3') and the profiles obtained via interpolation from 250,000 particles onto the grid and then averaged over horizontal planes (v_1', v_2', v_3') are shown. For a sufficiently accurate interpolation scheme the interpolated values (v_1', v_2', v_3') should be identical to the Eulerian values (u_1', u_2', u_3'). The results in the figure demonstrate that the fluctuating velocities are accurately resolved using 4th-order Lagrange polynomials.

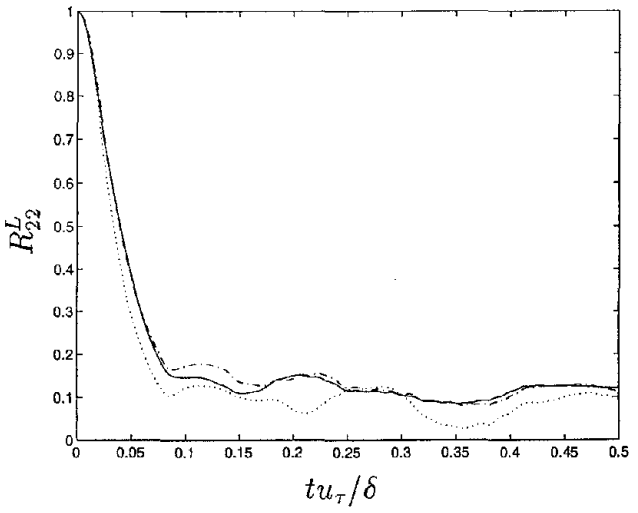

Figure 3: Effect of sample size on surface-normal component of Lagrangian velocity autocorrelation. ····· 1000 particles; —·— 2500 particles; —— 5000 particles. The autocorrelation shown in the figure is a representative result showing the differences obtained in Lagrangian statistics for different particle sample sizes. It is apparent from the figure that there is negligible difference between the correlation obtained using either 2500 or 5000 particles. Therefore, 5000 particles are used for measurement of Lagrangian statistical quantities.

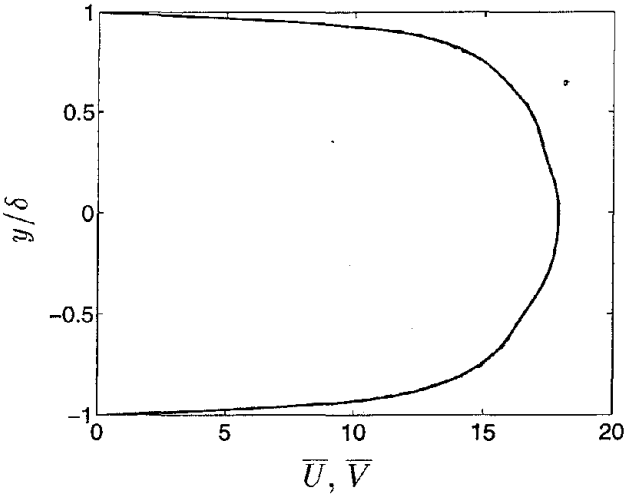

Figure 4: Effect of sample size on the mean velocity in turbulent channel flow. —— Eulerian (reference value); ---- 100,000 particles; —·— 250,000 particles; ····· 500,000 particles. The mean profile from the Eulerian calculation, $\overline{U}$, and the profiles obtained via interpolation from a specified number of particles onto the grid and then averaged over horizontal planes, $\overline{V}$, are shown. For a sufficiently large sample size the interpolated values $\overline{V}$ should be identical to the Eulerian value $\overline{U}$. The results in the figure demonstrate the mean profile is adequately resolved using 100,000 particles.

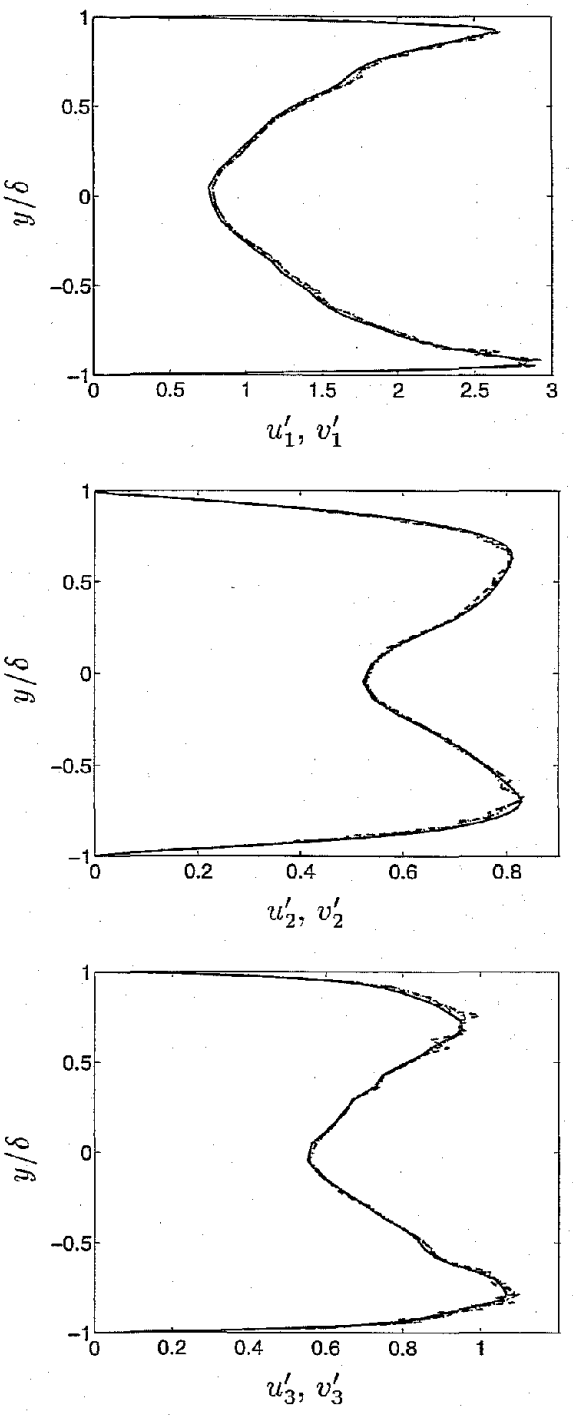

Figure 5: Effect of sample size on the fluctuating velocity in turbulent channel flow. —— Eulerian (reference value); ---- 100,000 particles; —·— 250,000 particles; ····· 500,000 particles. The profiles from the Eulerian calculation (u_1', u_2', u_3') and the profiles obtained via interpolation from a specified number of particles onto the grid and then averaged over horizontal planes (v_1', v_2', v_3') are shown. For a sufficiently large sample size the interpolated values (v_1', v_2', v_3') should be identical to the Eulerian values (u_1', u_2', u_3'). The results in the figure demonstrate the velocity fluctuations are adequately resolved using 250,000 particles.

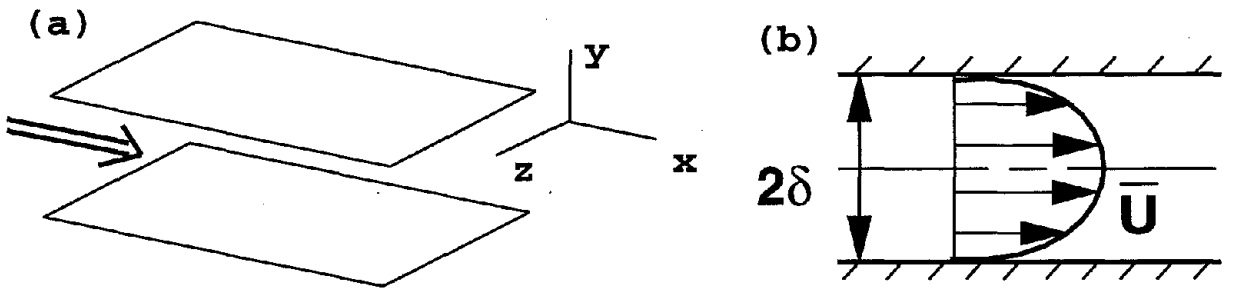

Figure 6: Schematic of fully-developed turbulent channel flow. Simulations were performed using resolutions of $64 \times 65 \times 64$ grid points. (a) three-dimensional perspective showing main flow direction aligned with x (streamwise) axis, the spanwise direction is aligned with the z axis, the wall-normal direction aligned with the y axis. (b) x-y cross-section showing mean velocity profile $\overline{U}$ between channel walls separated by a distance of 2δ.

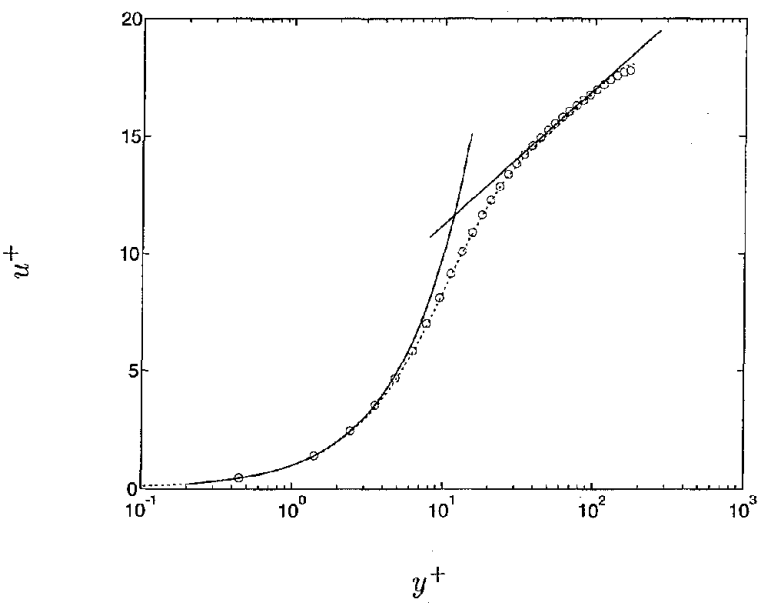

Figure 7: Mean velocity profile in turbulent channel flow. $u^+ = \overline{U}/\sqrt{\tau_w/\rho}$ where $\tau_{1,w}$ = wall shear stress, $y^+ = y\sqrt{\tau_{1,w}/(\nu_1^2\rho_1)}$. LES predictions (shown using ---- line) obtained at same Reynolds number as in Kim *et al.* (1987) (shown using o).

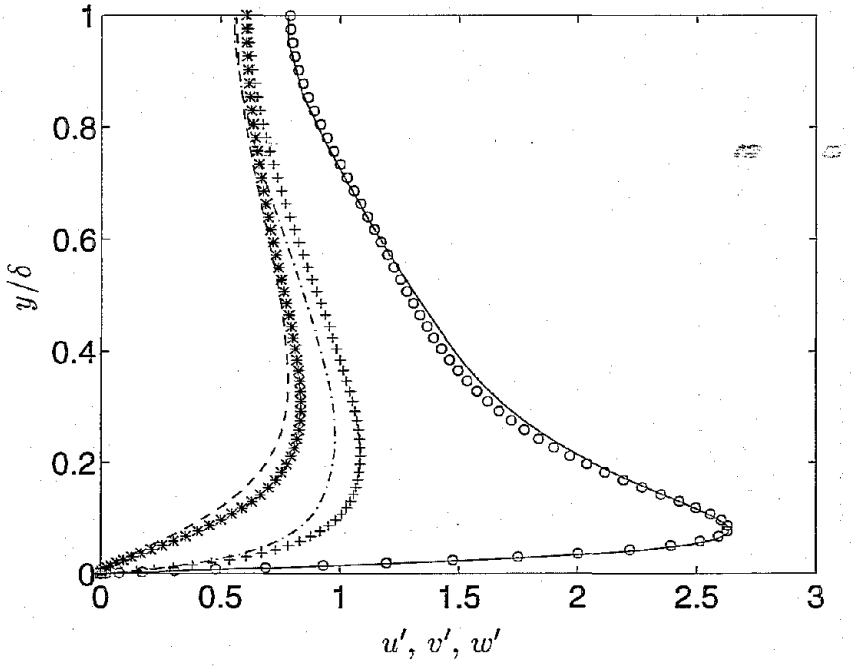

Figure 8: Comparison of root-mean-square velocity fluctuations from LES of turbulent channel flow to Kim *et al.* (1987). LES: —— streamwise (u'); ---- wall-normal (v'); —·— spanwise (w'); Kim *et al.* (1987): ∘ streamwise (u'); ∗ wall-normal (v'); + spanwise (w').

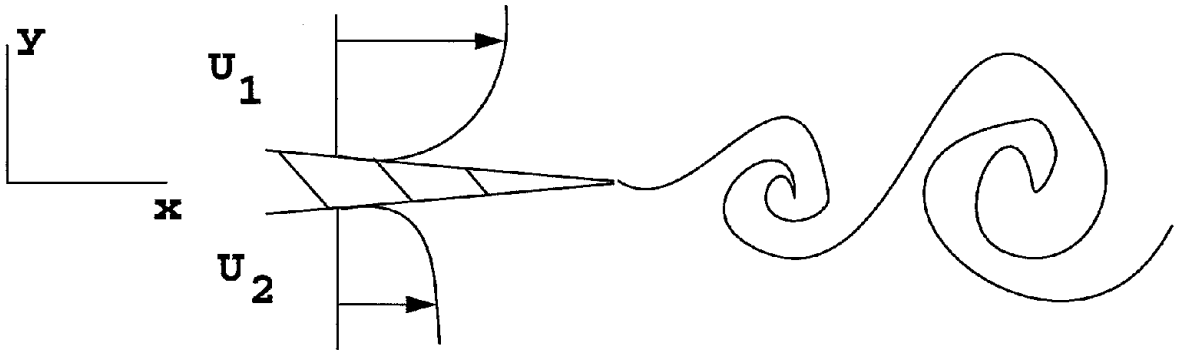

Figure 9: Schematic of turbulent mixing layer. Simulations were performed using resolutions of $64 \times 65 \times 128$ grid points in the x, y, and z directions, respectively. The layer grows with increasing streamwise distance.

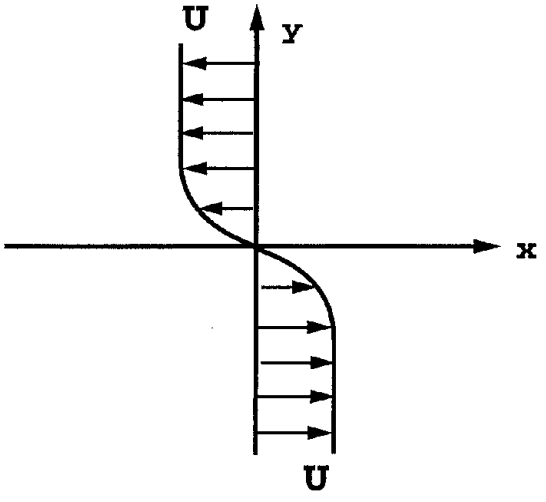

Figure 10: Schematic velocity profile of temporally evolving turbulent mixing layer. Coordinate system translates at the convection velocity of the layer (one-half the sum of the upper and lower stream speeds).

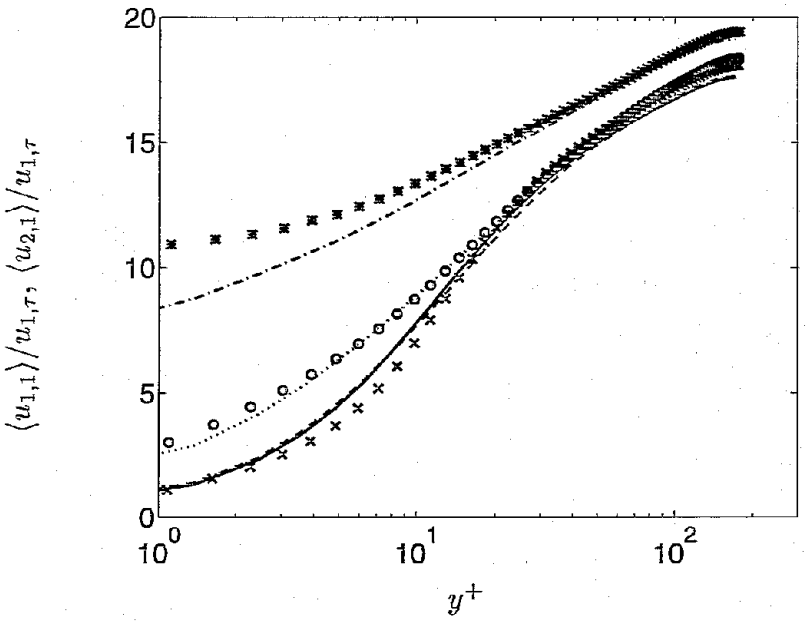

(*a*)

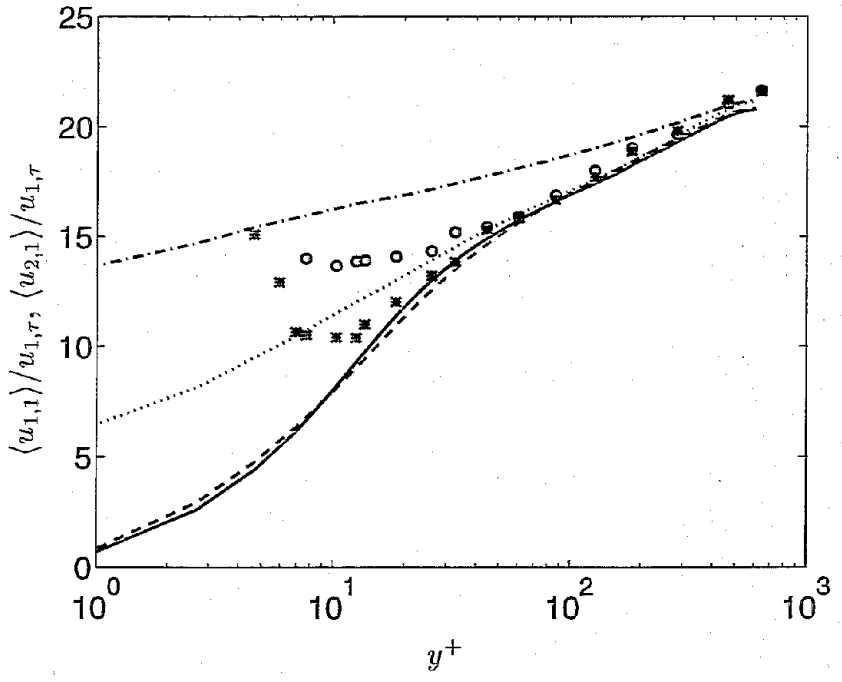

(*b*)

Figure 11: Mean streamwise velocity in turbulent channel flow. (*a*) $Re_\tau = 180$; (*b*) $Re_\tau = 644$. LES: —— fluid elements; ---- Lycopodium; ····· 50μm glass; —·— copper; Rouson & Eaton (1994) (in *a*) and Kulick *et al.* (1994) (in *b*): × Lycopodium; ∘ 50μm glass; ∗ copper.

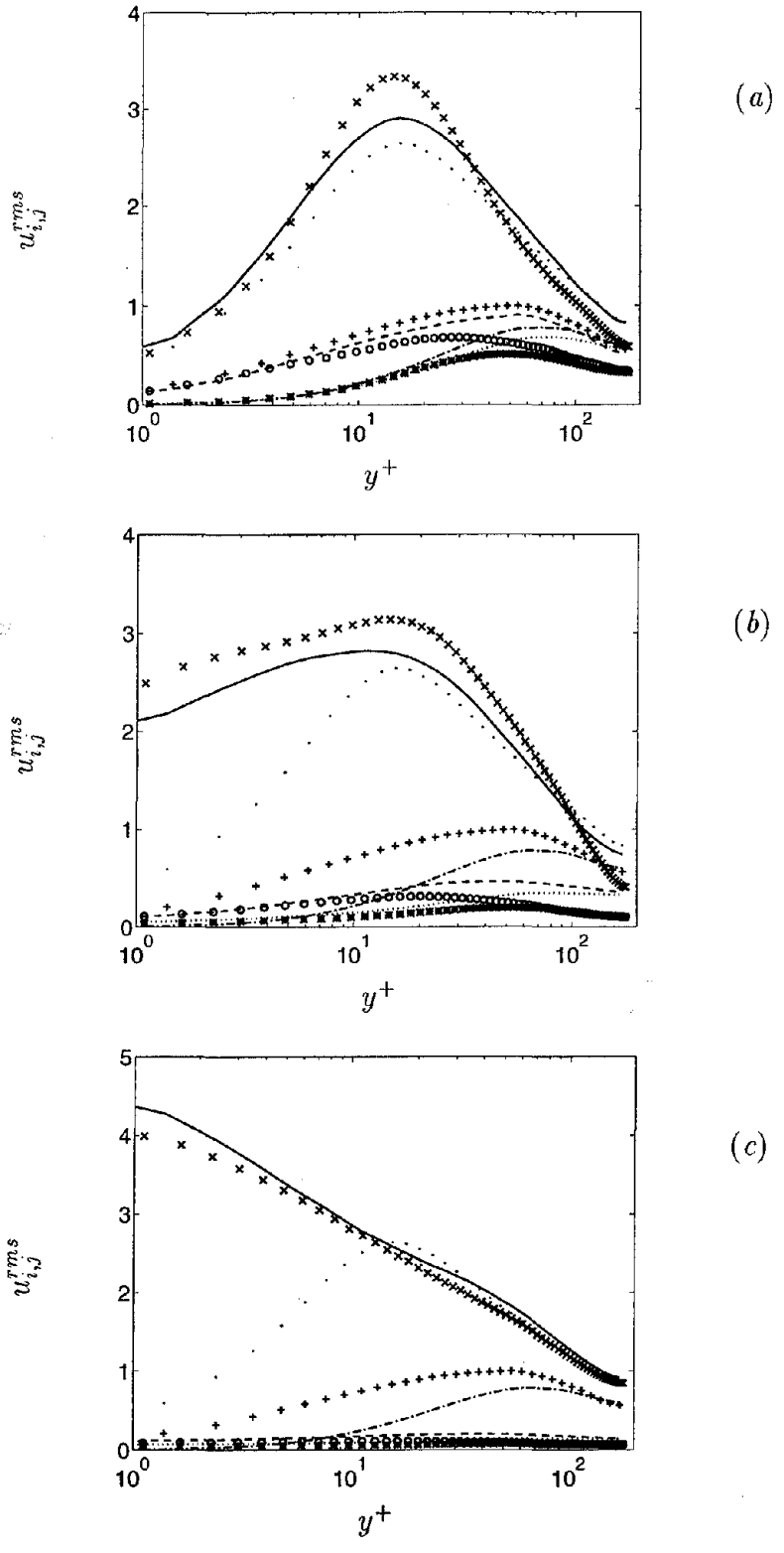

Figure 12: Root-mean-square velocity fluctuations in turbulent channel flow, $Re_\tau = 180$. (*a*) Lycopodium; (*b*) 50μm glass; (*c*) copper. LES fluid: • $i = 1$; —·— $i = 2$; + $i = 3$; LES particle: —— $i = 1$; ····· $i = 2$; ---- $i = 3$; particle fluctuations from Rouson & Eaton (1994): × $i = 1$; ∗ $i = 2$; ∘ $i = 3$.

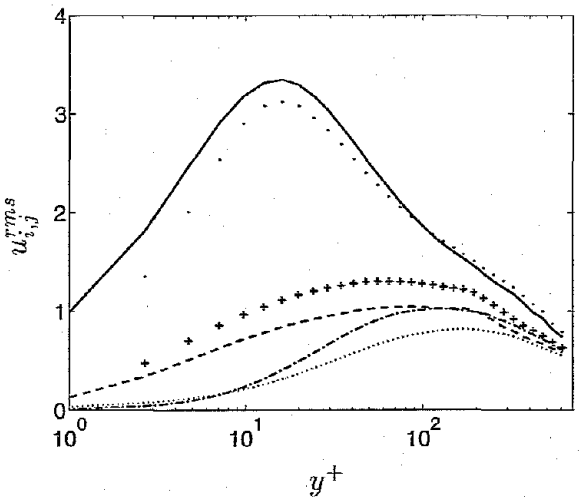

Figure 13: Root-mean-square velocity fluctuations in turbulent channel flow, $Re_\tau = 644$. (*a*) Lycopodium; (*b*) 50μm glass; (*c*) copper. LES fluid: • $i = 1$; —·— $i = 2$; + $i = 3$; LES particle: —— $i = 1$; ····· $i = 2$; ---- $i = 3$; particle fluctuations from Kulick *et al.* (1994): $\times$ $i = 1$; $*$ $i = 2$.

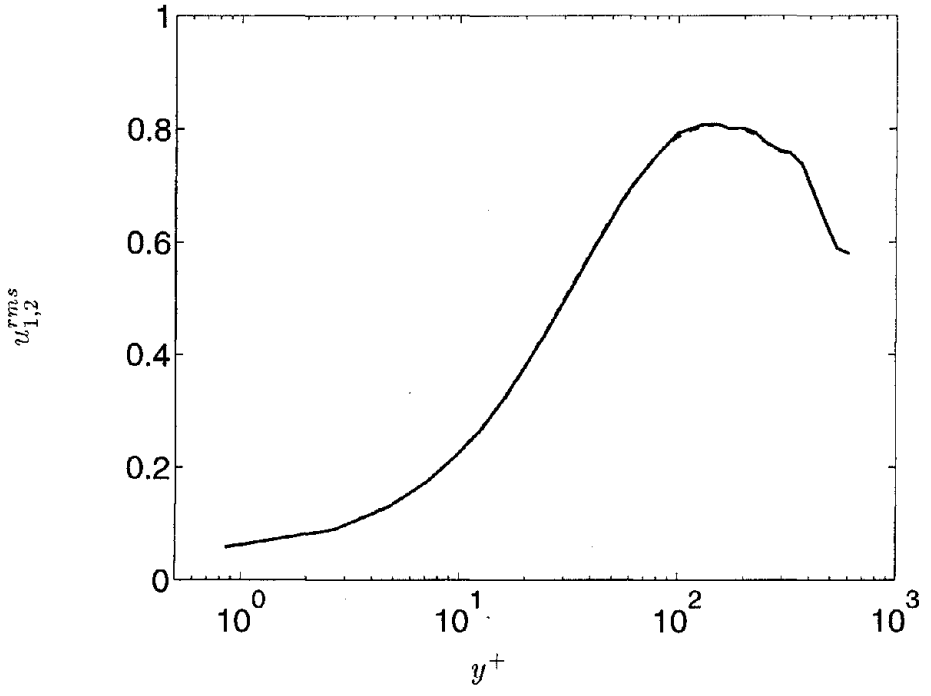

Figure 14: Wall-normal velocity fluctuations for 28μm Lycopodium particles, $Re_\tau = 644$. —— without SGS velocity in particle equation of motion; ---- with SGS velocity in particle equation of motion.

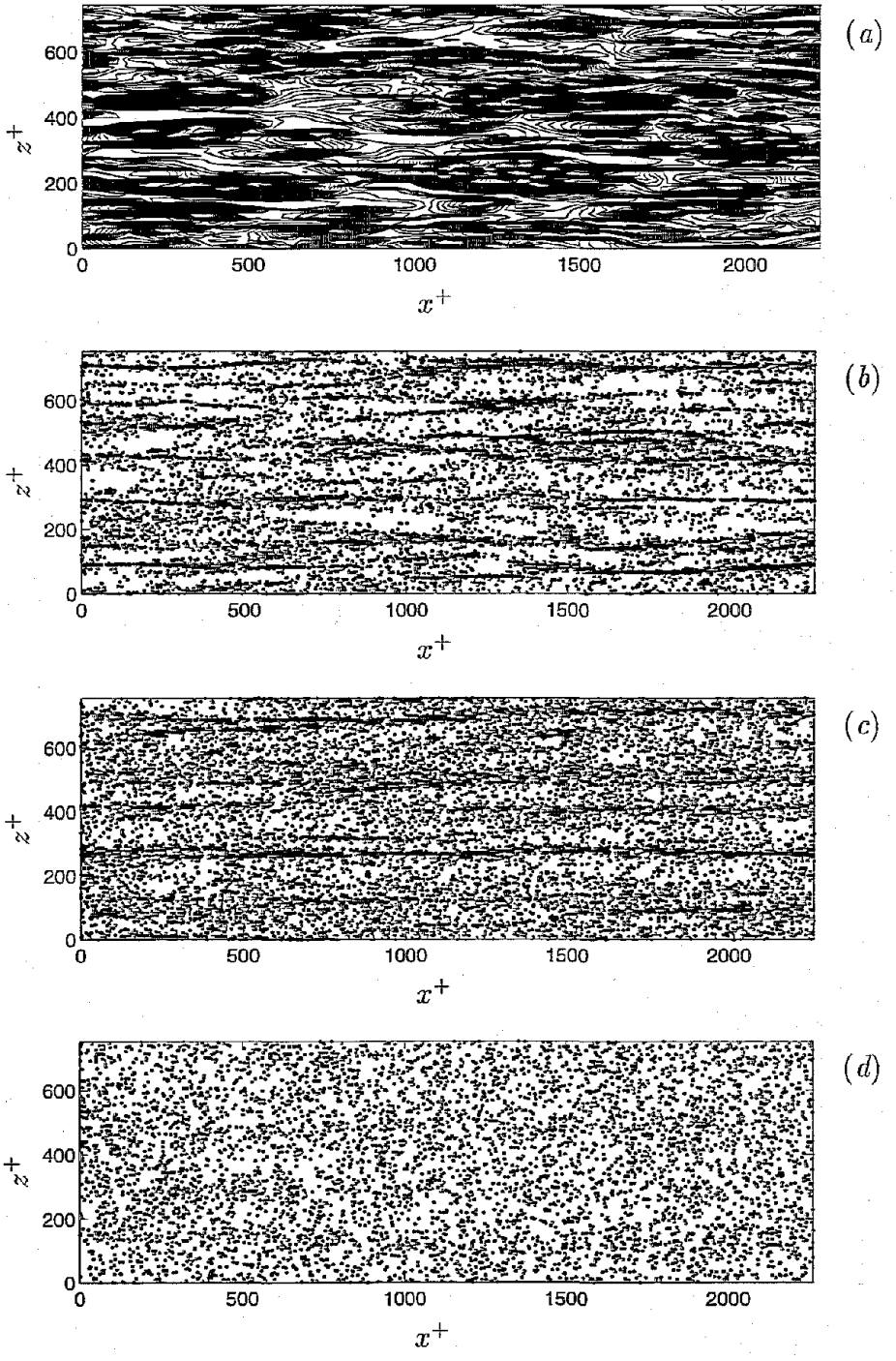

Figure 15: Velocity contours and particle distributions from LES at $t = 6\delta/u_\tau$, $y^+ = 3.6$, $Re_\tau = 180$. (a) streamwise velocity; (b) 28μm Lycopodium; (c) 50μm glass; (d) 70μm copper.

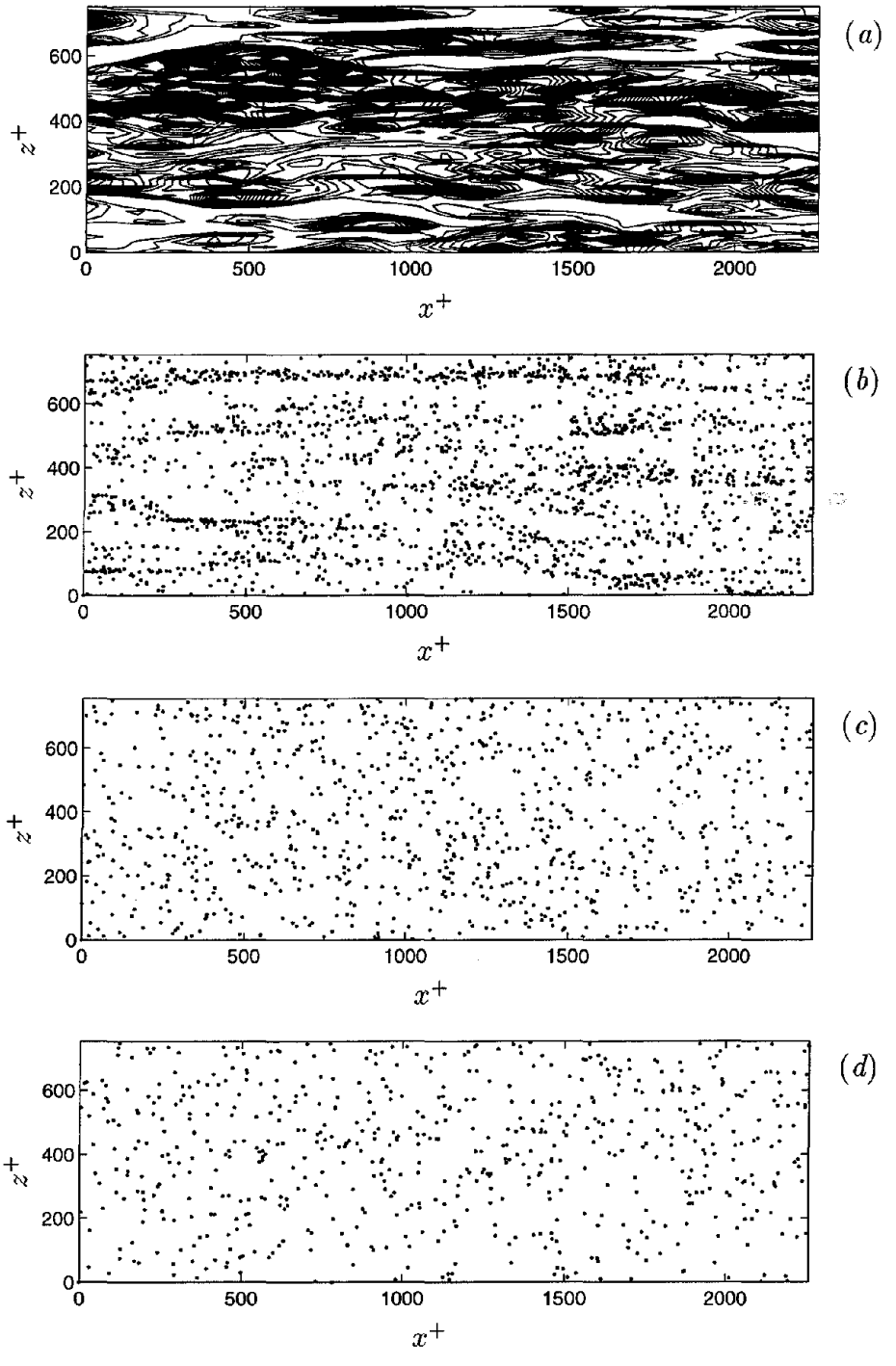

Figure 16: Velocity contours and particle distributions from LES at $t = 3\delta/u_\tau$, $y^+ = 4.8$, $Re_\tau = 644$. (a) streamwise velocity; (b) 28μm Lycopodium; (c) 50μm glass; (d) 70μm copper.

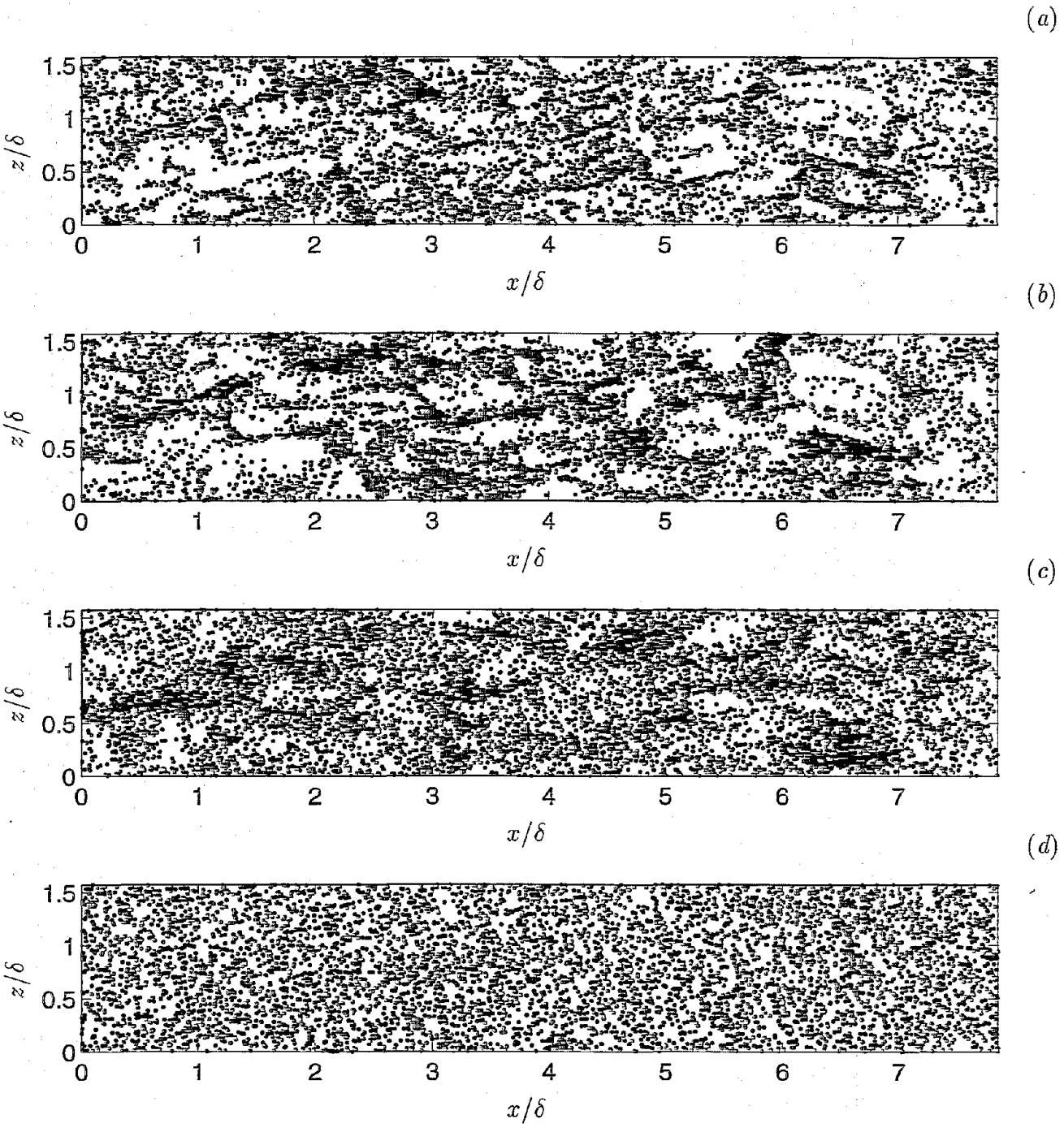

Figure 17: Particle distribution for the region $0.975 \leq y/\delta < 1.025$ at $t = 2\delta/u_\tau$, $Re_\tau = 644$. (*a*) 28μm Lycopodium; (*b*) 25μm glass; (*c*) 50μm glass; (*d*) 70μm copper.

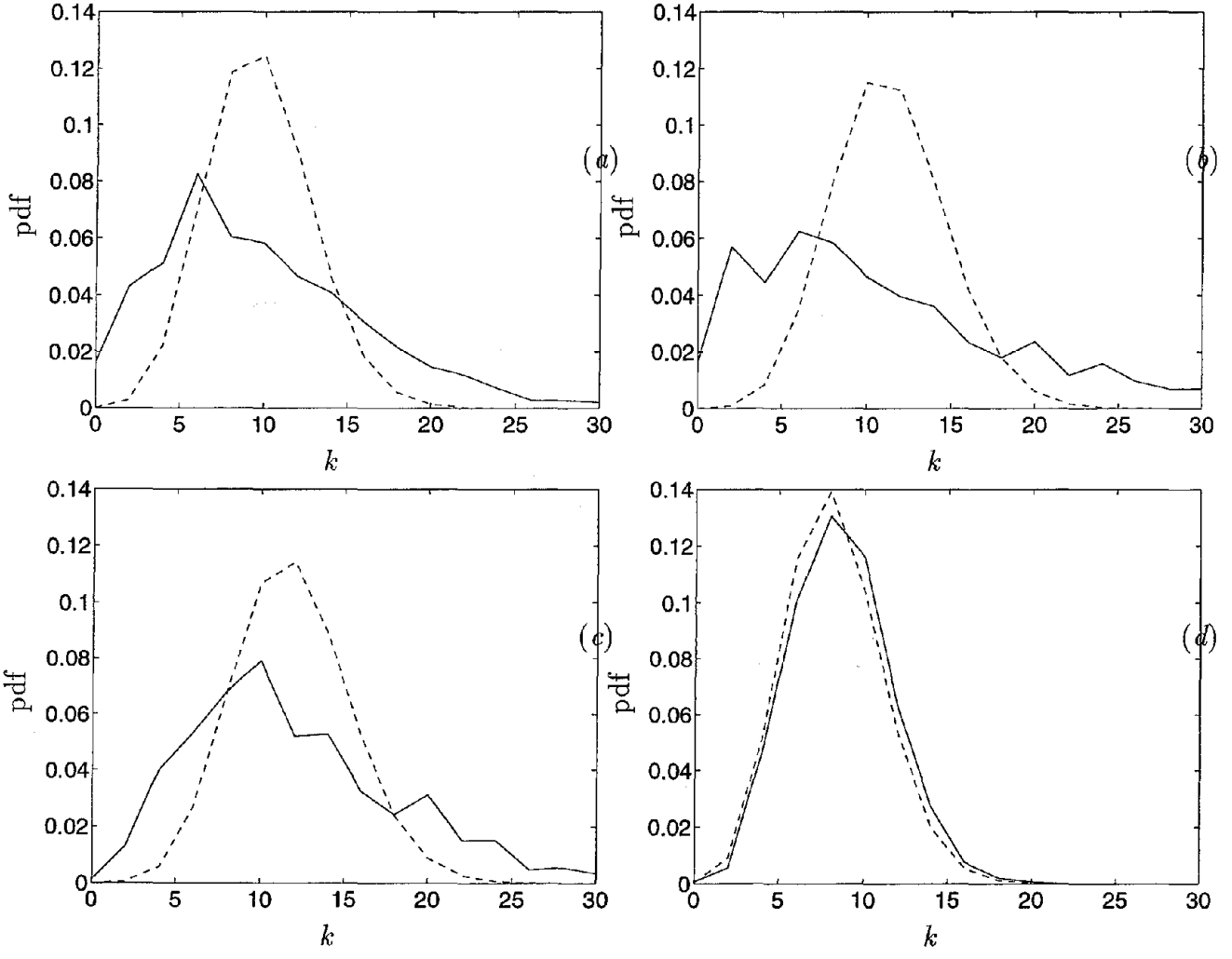

Figure 18: Probability distribution function of particle number density in $0.975 \leq y/\delta < 1.025$ at $t = 2\delta/u_\tau$, $Re_\tau = 644$. Cell size used for calculation of pdf is 2.6mm. (a) 28μm Lycopodium; (b) 25μm glass; (c) 50μm glass; (d) 70μm copper.

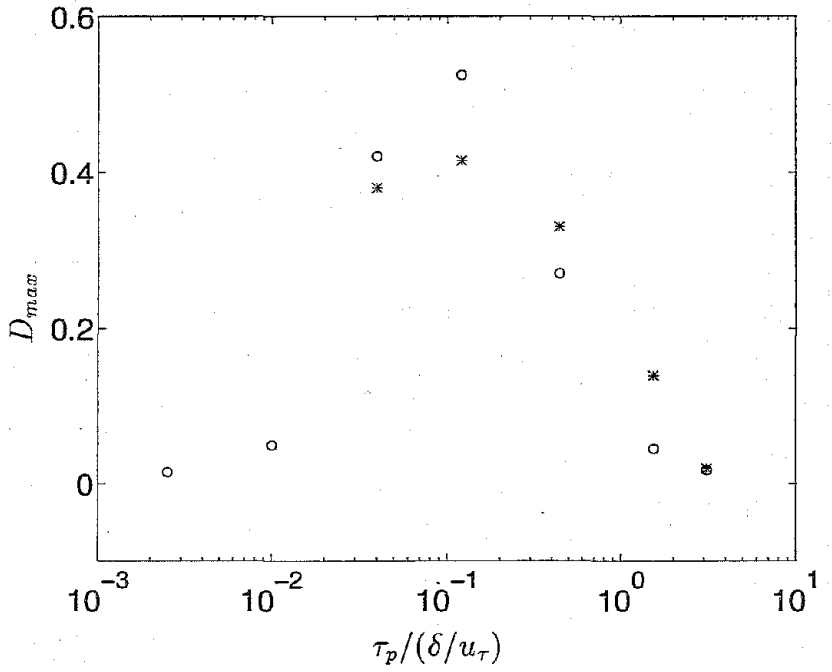

Figure 19: Maximum values of D as defined in Fessler *et al.* (1994) for particles in the region $0.975 \leq y/\delta < 1.025$, $Re_\tau = 644$. ∘ LES; ∗ Fessler *et al.* (1994).

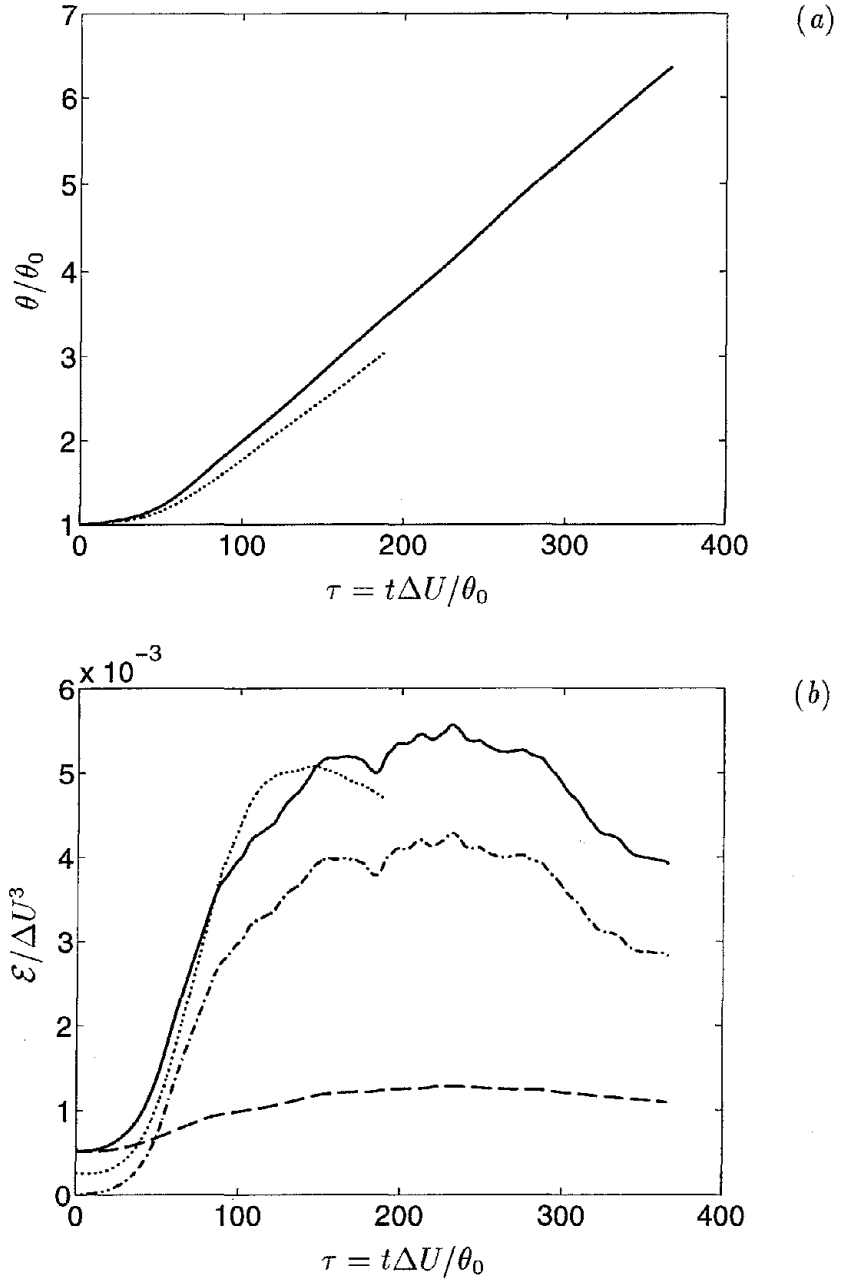

Figure 20: Temporal evolution of momentum thickness θ and dissipation rate $\mathcal{E}$. (a) momentum thickness; (b) dissipation rate. In (a) —— LES; ····· Rogers & Moser (1994). In (b) LES: —— $\mathcal{E}$; ---- molecular dissipation $\int_{-\infty}^{\infty} \nu \langle |S|^2 \rangle_{xz} dy$; —·— SGS dissipation $\int_{-\infty}^{\infty} \langle \nu_T |S|^2 \rangle_{xz} dy$; ····· Rogers & Moser (1994).

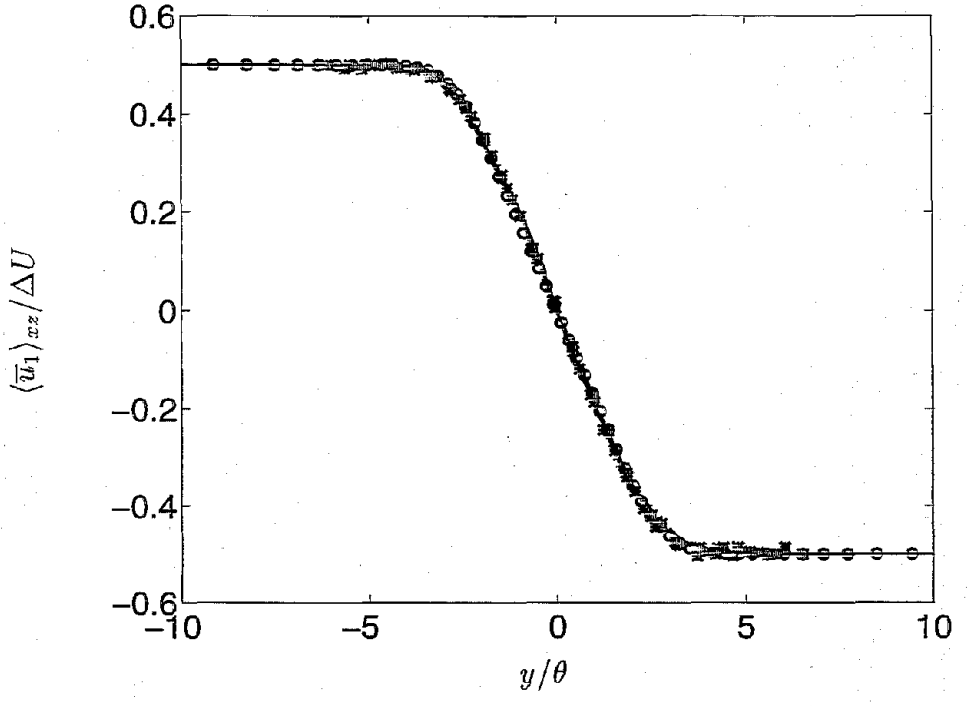

Figure 21: Fluid mean velocity. LES: —— $t\Delta U/\theta_0 = 167$; ---- $t\Delta U/\theta_0 = 202$; —·— $t\Delta U/\theta_0 = 237$; ····· $t\Delta U/\theta_0 = 272$. ∘ Rogers & Moser (1994); ∗ Bell & Mehta (1990).

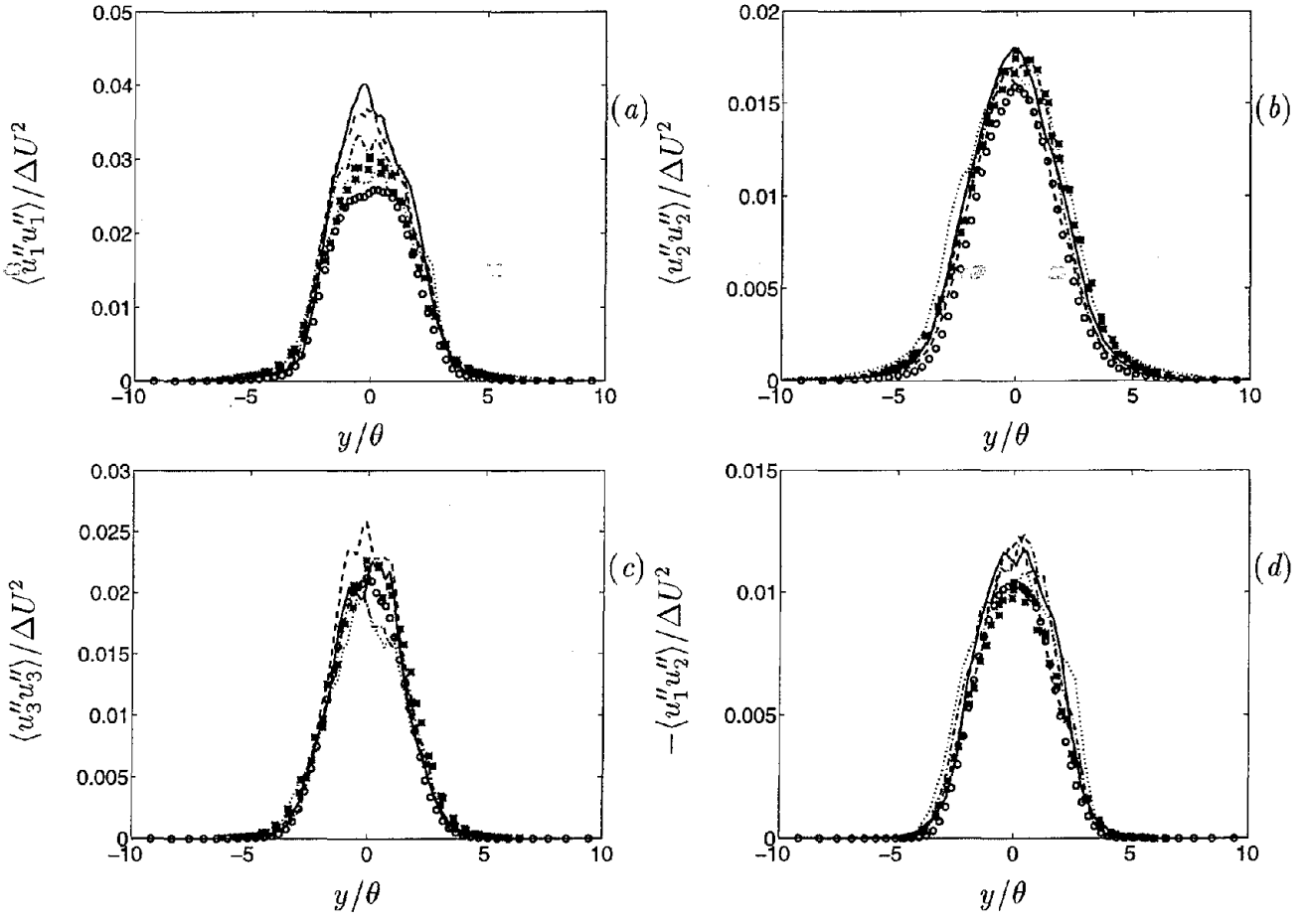

Figure 22: Fluid Reynolds stresses LES: —— $t\Delta U/\theta_0 = 167$; ---- $t\Delta U/\theta_0 = 202$; —·— $t\Delta U/\theta_0 = 237$; ····· $t\Delta U/\theta_0 = 272$. ∘ Rogers & Moser (1994); ∗ Bell & Mehta (1990).

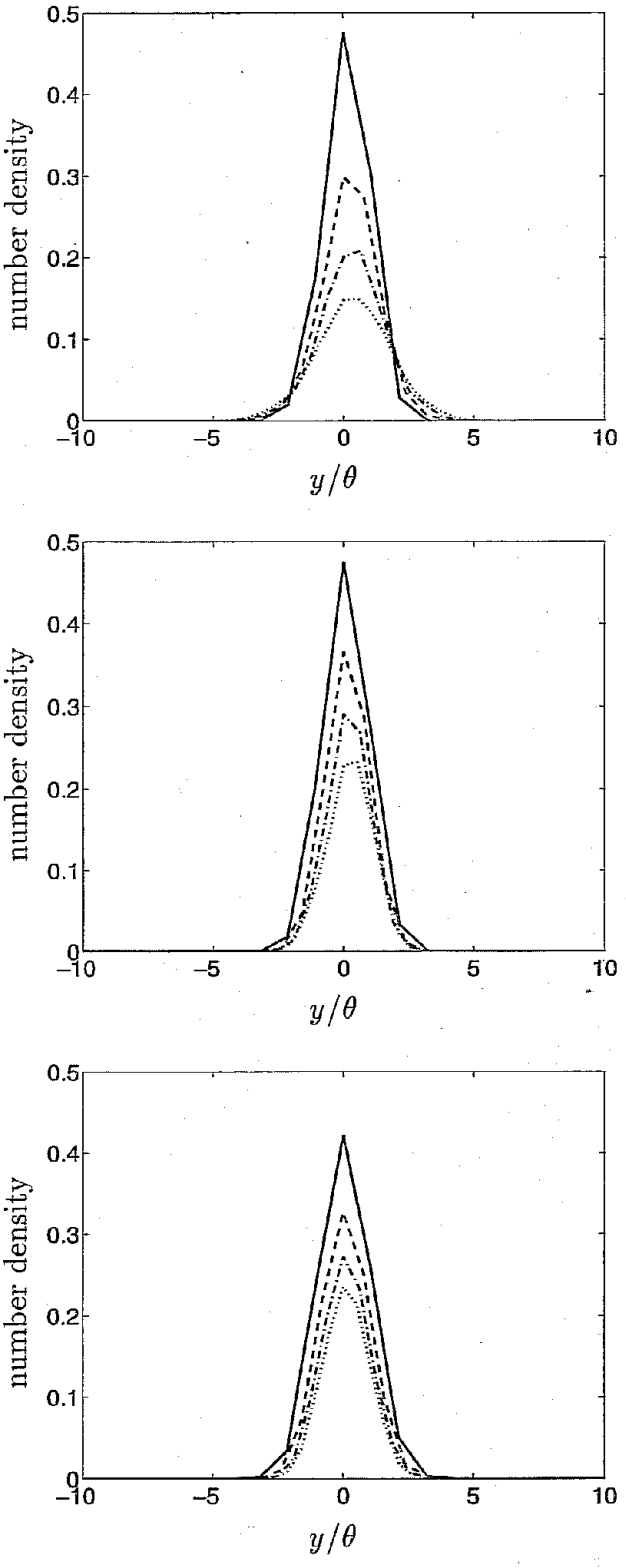

Figure 23: Evolution of the particle number density field (normalized by the total number of particles). —— $X = 100$mm ($\tau = 168$); ---- $X = 150$mm ($\tau = 236$); —·— $X = 200$mm ($\tau = 300$); ····· $X = 250$mm ($\tau = 362$). Particle diameter: (a) 42μm; (b) 72μm; (c) 135μm.

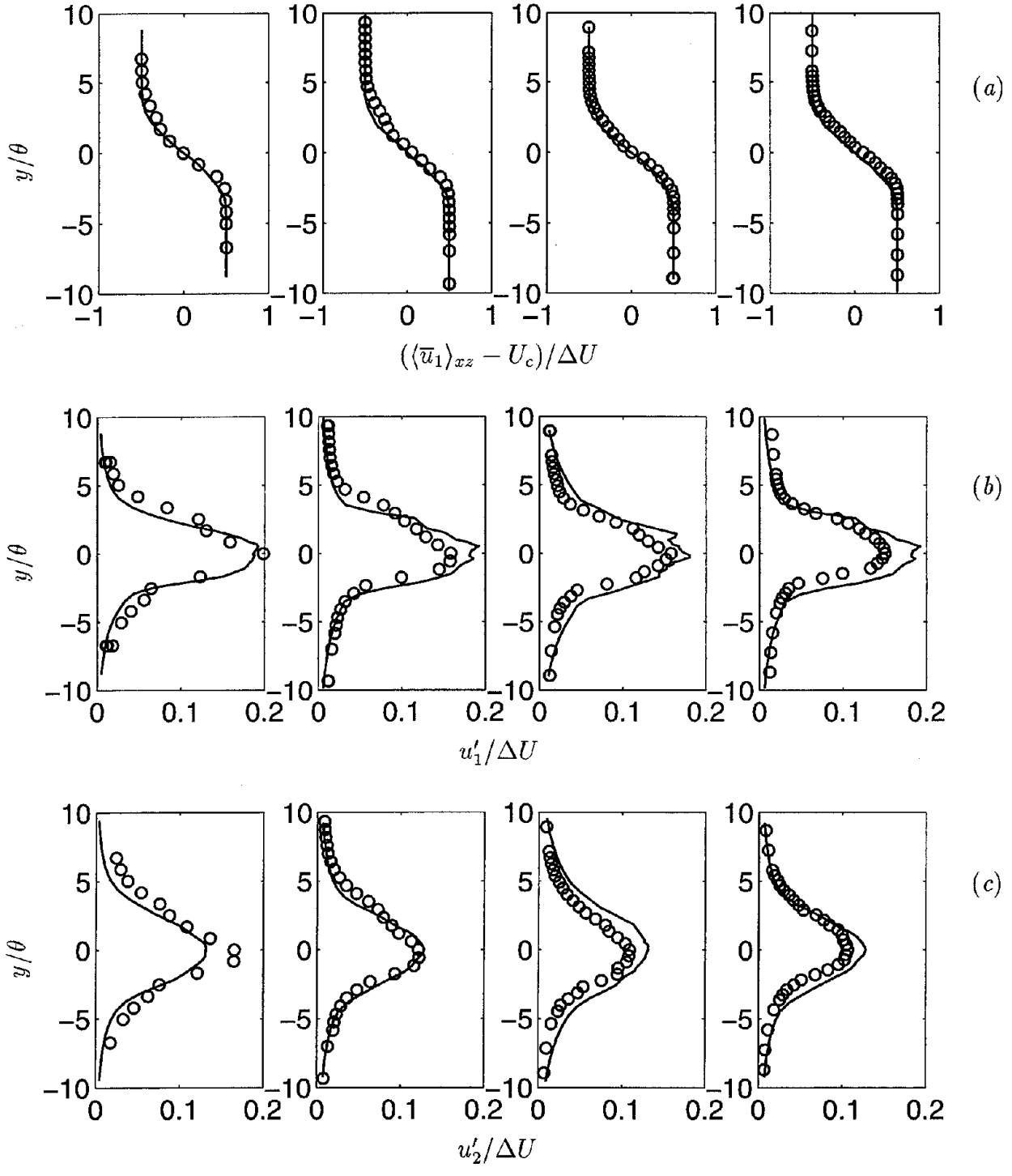

Figure 24: Comparison of fluid velocity from LES and Hishida *et al.* (1992). (*a*) mean streamwise velocity; (*b*) rms streamwise velocity fluctuations; (*c*) rms cross-stream velocity fluctuations. First column: $X = 100$mm ($\tau = 168$); second column: $X = 150$mm ($\tau = 236$); third column: $X = 200$mm ($\tau = 300$); fourth column: $X = 250$mm ($\tau = 362$). —— LES; o Hishida *et al.* (1992).

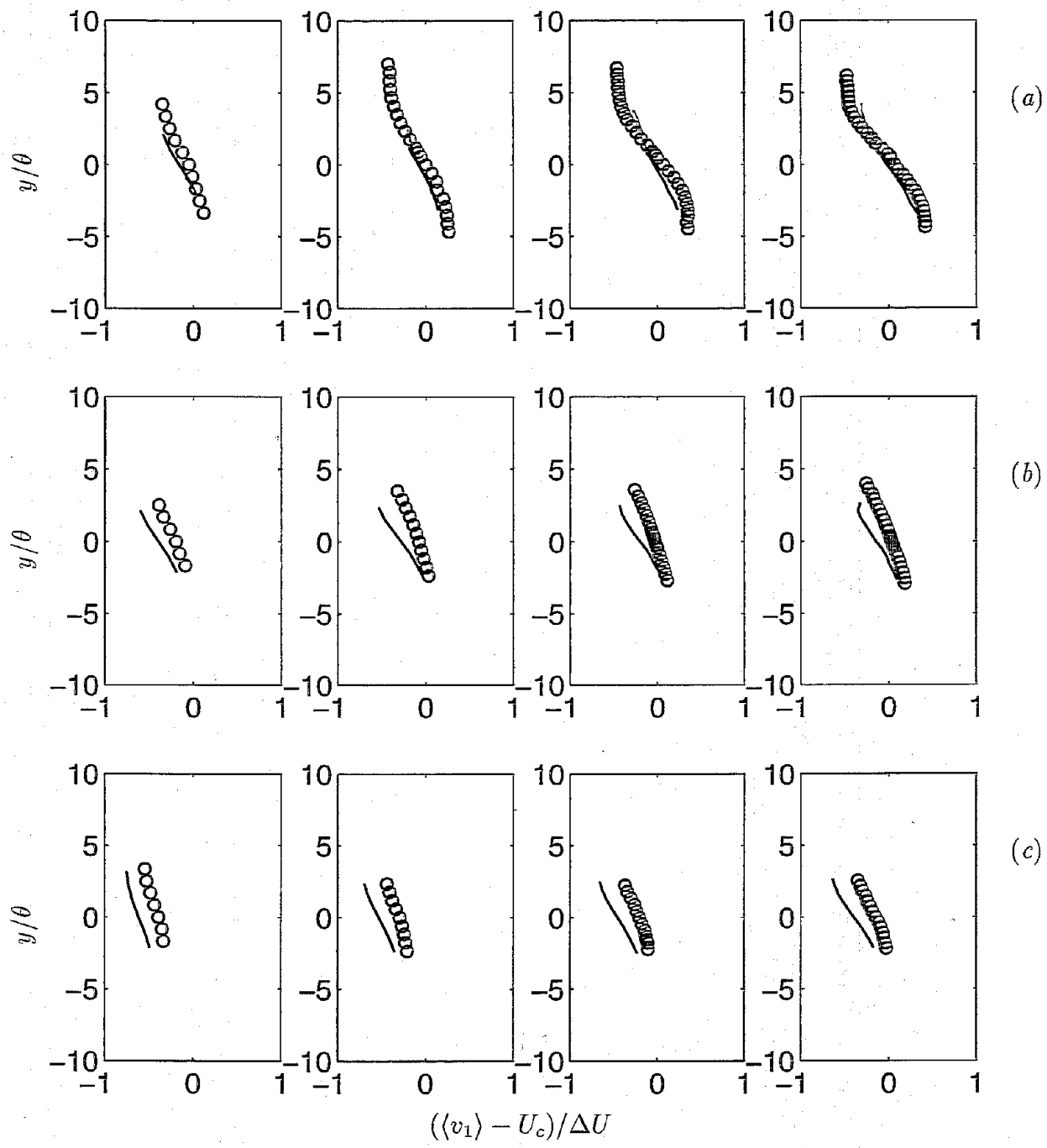

Figure 25: Comparison of particle mean streamwise velocity from LES and Hishida *et al.* (1992). (*a*) 42μm particle; (*b*) 72μm particle; (*c*) 135μm particle. First column: $X = 100$mm ($\tau = 168$); second column: $X = 150$mm ($\tau = 236$); third column: $X = 200$mm ($\tau = 300$); fourth column: $X = 250$mm ($\tau = 362$). —— LES; o Hishida *et al.* (1992).

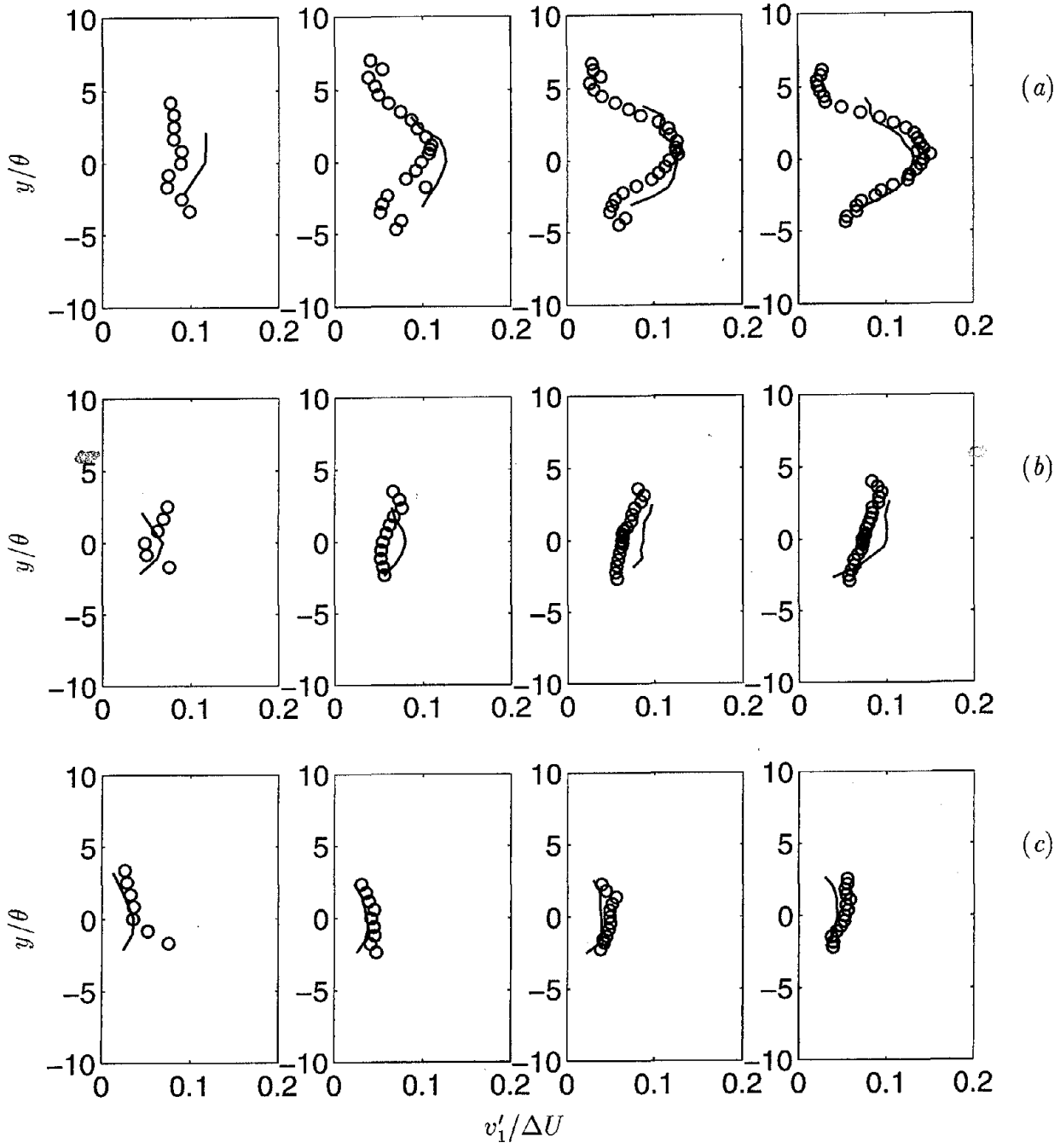

Figure 26: Comparison of rms streamwise particle velocity fluctuations from LES and Hishida *et al.* (1992). (*a*) 42μm particle; (*b*) 72μm particle; (*c*) 135μm particle. First column: X = 100mm (τ = 168); second column: X = 150mm (τ = 236); third column: X = 200mm (τ = 300); fourth column: X = 250mm (τ = 362). —— LES; ○ Hishida *et al.* (1992).

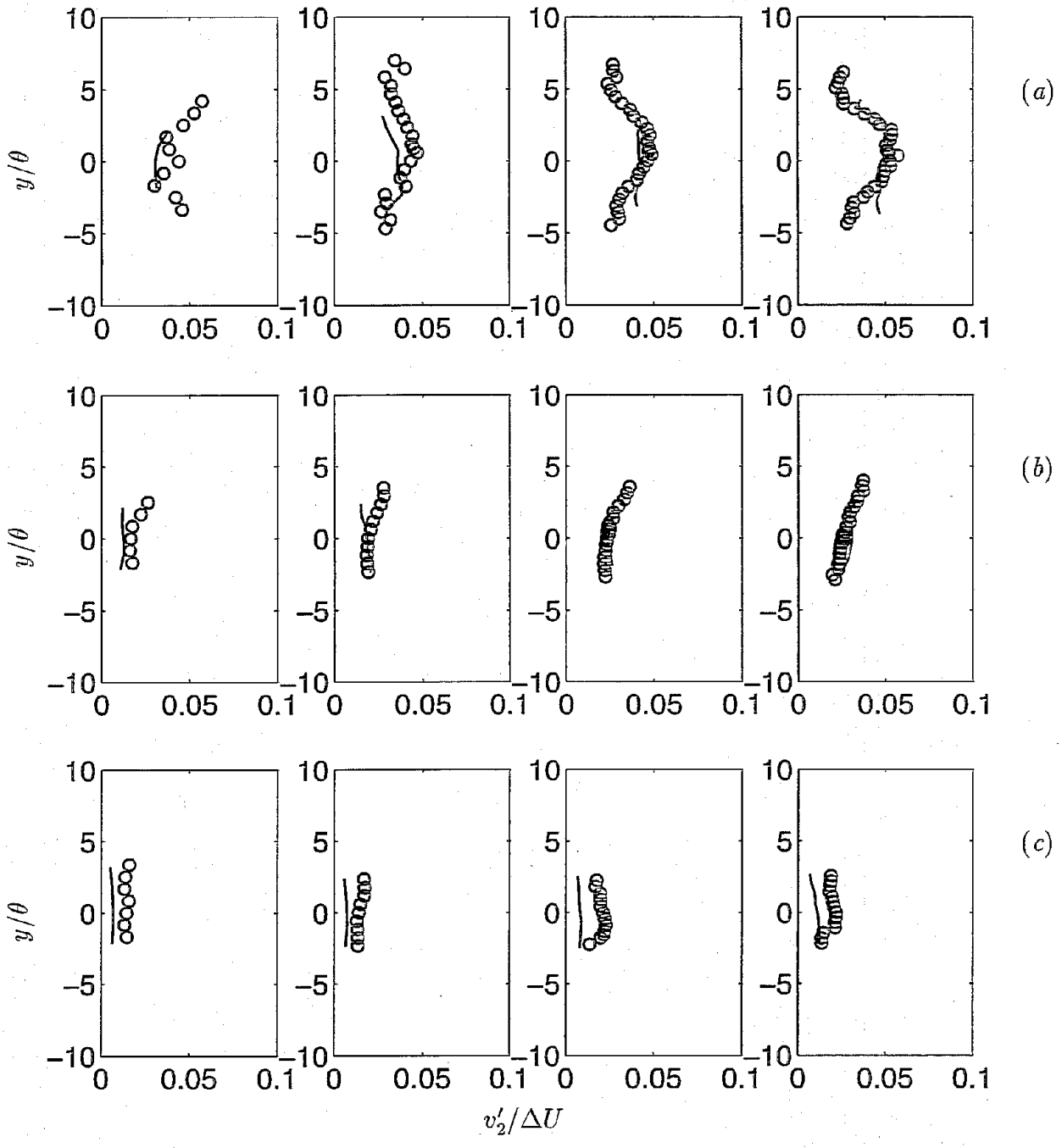

Figure 27: Comparison of rms cross-stream particle velocity fluctuations from LES and Hishida *et al.* (1992). (*a*) 42μm particle; (*b*) 72μm particle; (*c*) 135μm particle. First column: $X = 100$mm ($\tau = 168$); second column: $X = 150$mm ($\tau = 236$); third column: $X = 200$mm ($\tau = 300$); fourth column: $X = 250$mm ($\tau = 362$). —— LES; ○ Hishida *et al.* (1992).

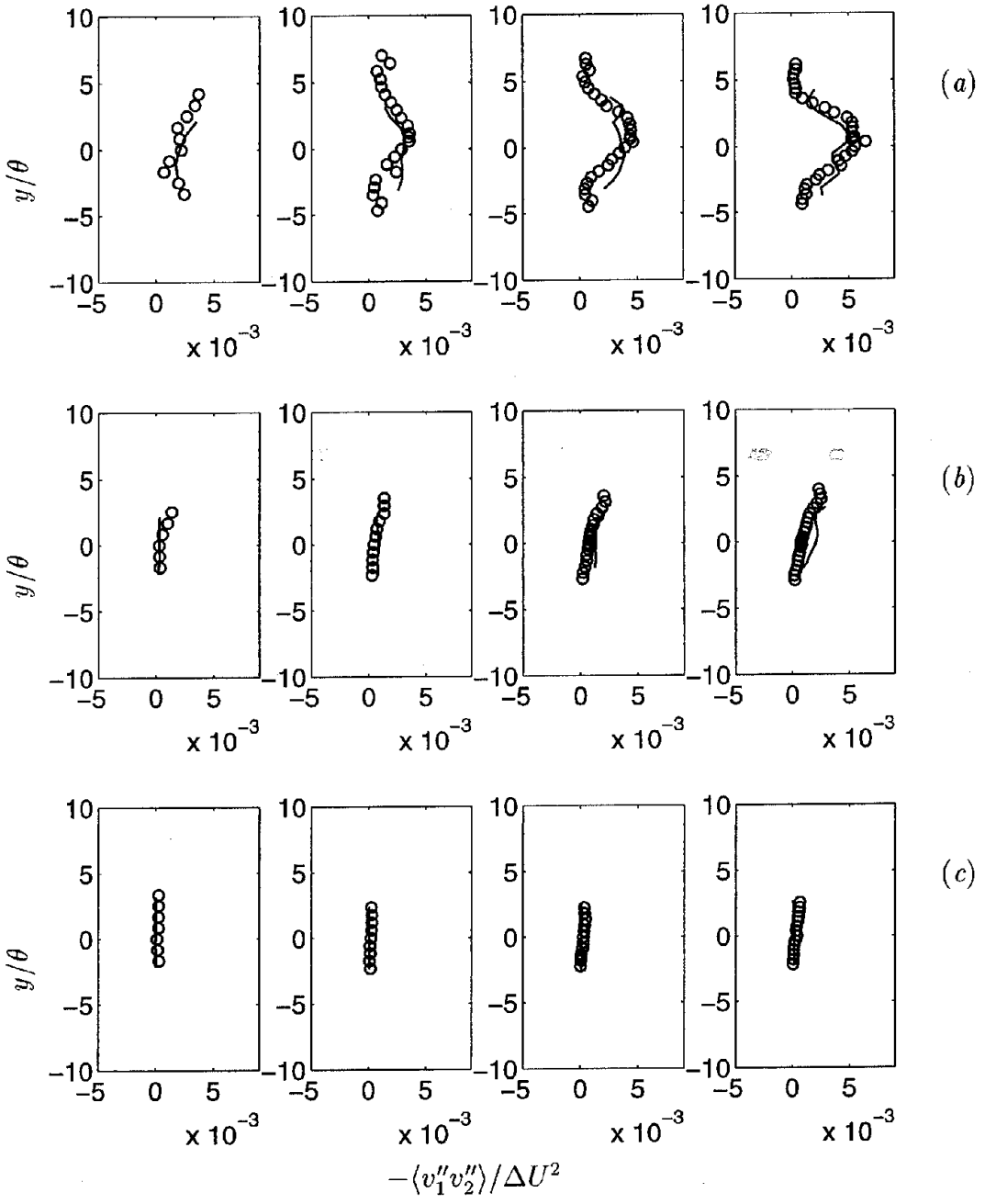

Figure 28: Comparison of particle velocity correlations from LES and Hishida *et al.* (1992). (*a*) 42μm particle; (*b*) 72μm particle; (*c*) 135μm particle. First column: X = 100mm (τ = 168); second column: X = 150mm (τ = 236); third column: X = 200mm (τ = 300); fourth column: X = 250mm (τ = 362). —— LES; o Hishida *et al.* (1992).

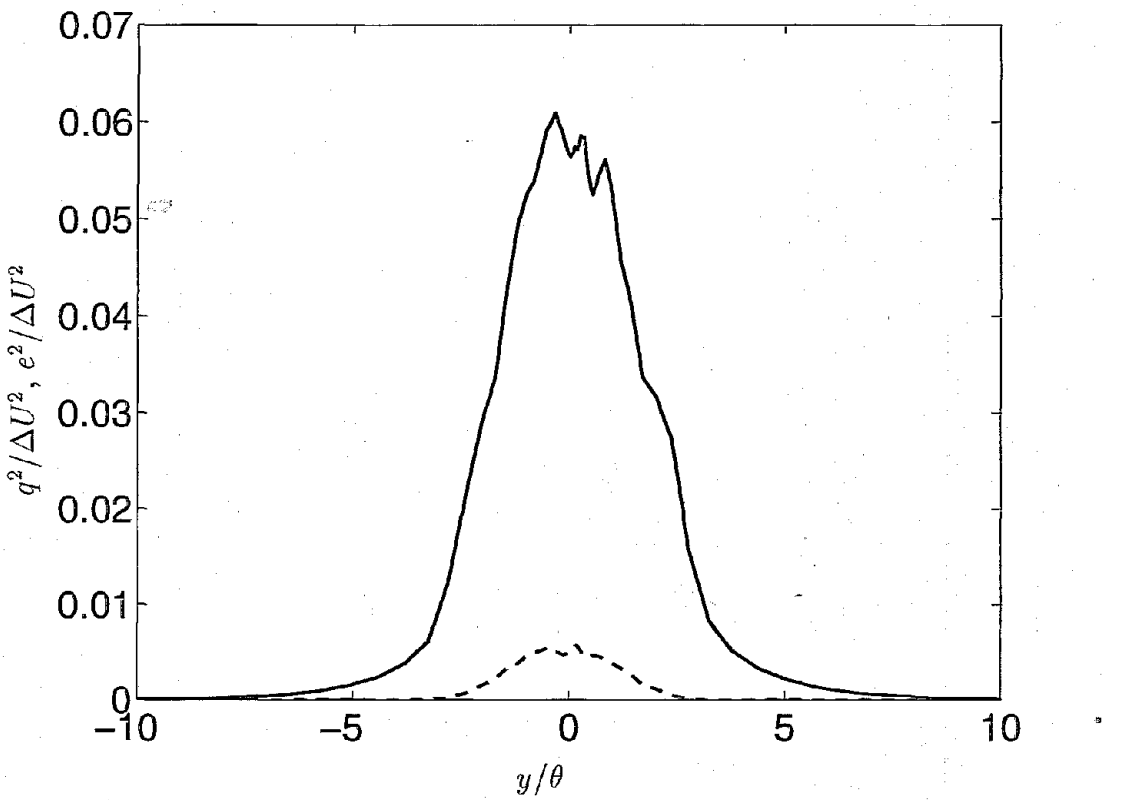

Figure 29: Cross-stream profile of SGS energy q^2 and resolved turbulent kinetic energy e^2 at $X = 200\text{mm}$ ($\tau = 300$). —— $e^2/\Delta U^2$; ---- $q^2/\Delta U^2$.

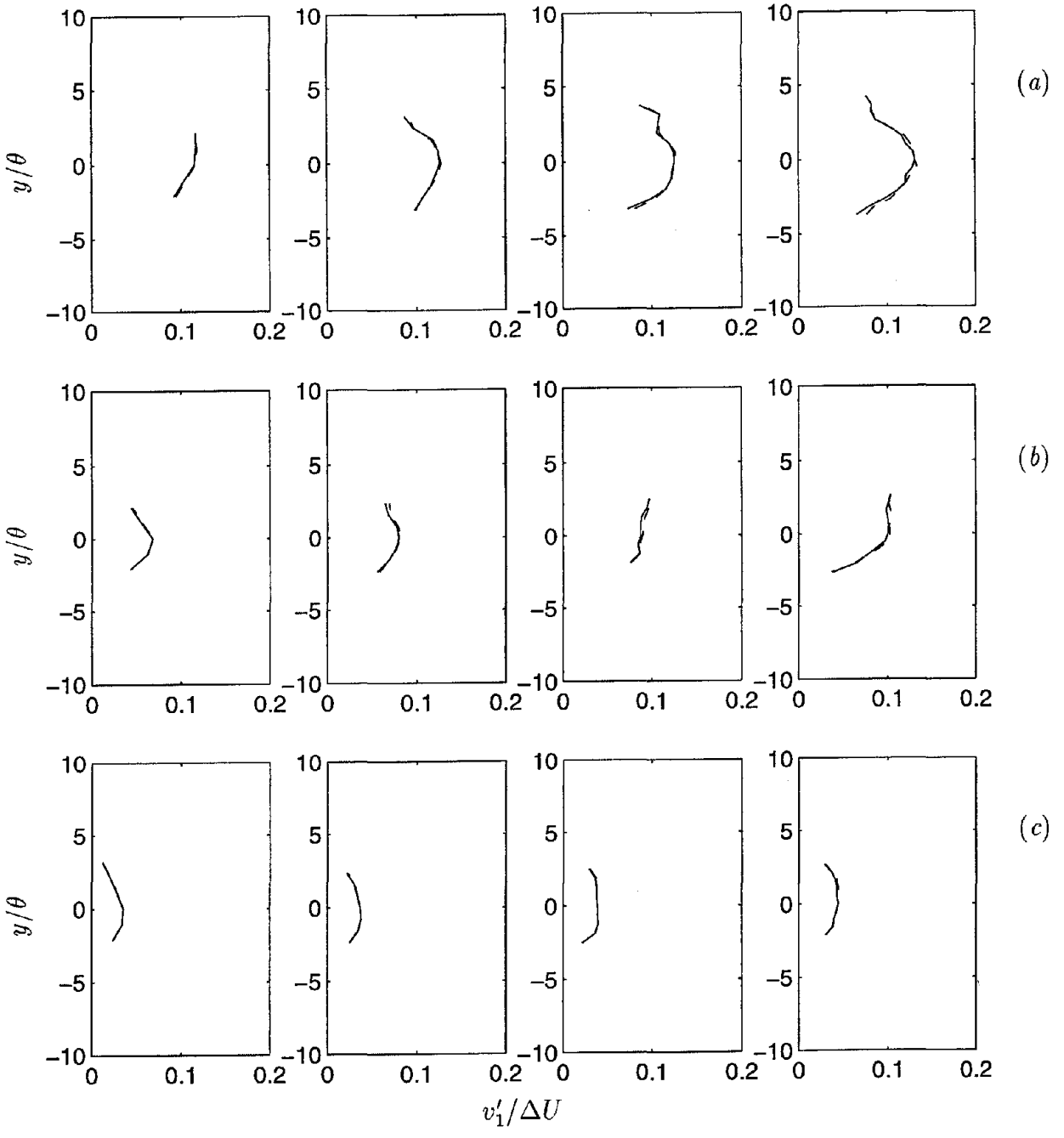

Figure 30: Comparison of particle rms streamwise velocity fluctuations with and without SGS velocity fluctuations. (a) 42μm particle; (b) 72μm particle; (c) 135μm particle. First column: X = 100mm (τ = 168); second column: X = 150mm (τ = 236); third column: X = 200mm (τ = 300); fourth column: X = 250mm (τ = 362). —— without SGS model; ---- with SGS model.

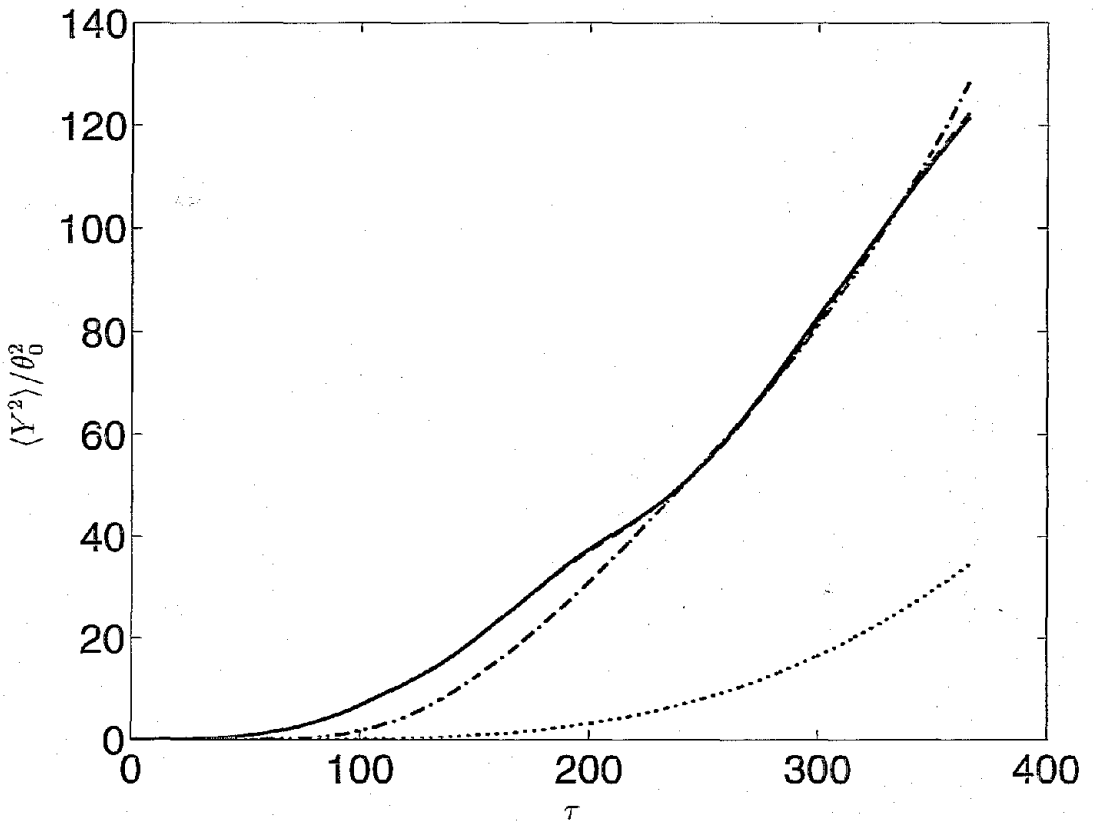

Figure 31: Mean-square particle dispersion. —— fluid; ---- 1.5μm; —·— 36μm; ····· 95μm.

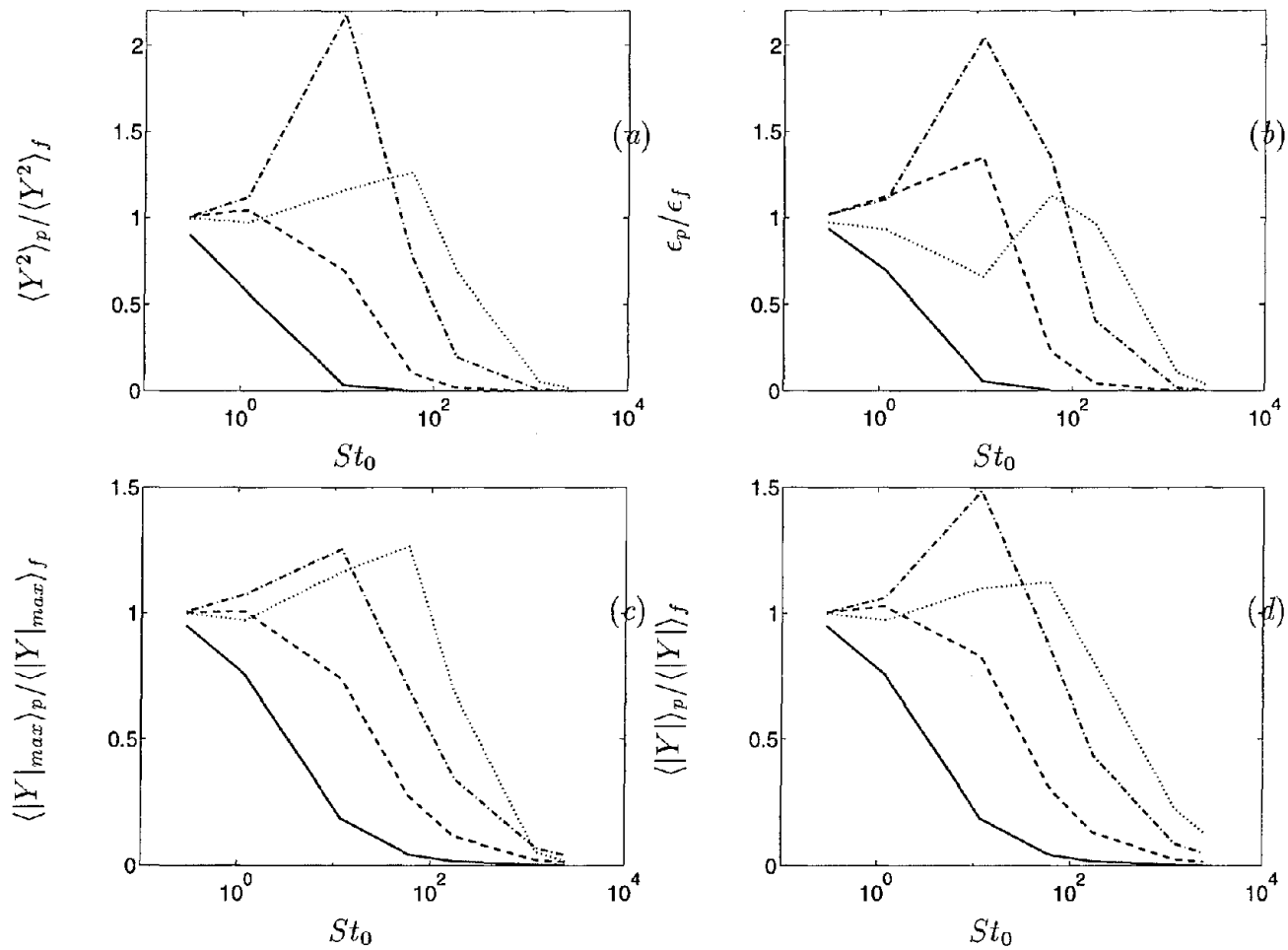

Figure 32: Measures of particle dispersion as a function of Stokes number defined using initial vorticity thickness. —— $\tau = 8$; ---- $\tau = 50$; —·— $\tau = 91$; ····· $\tau = 166$.

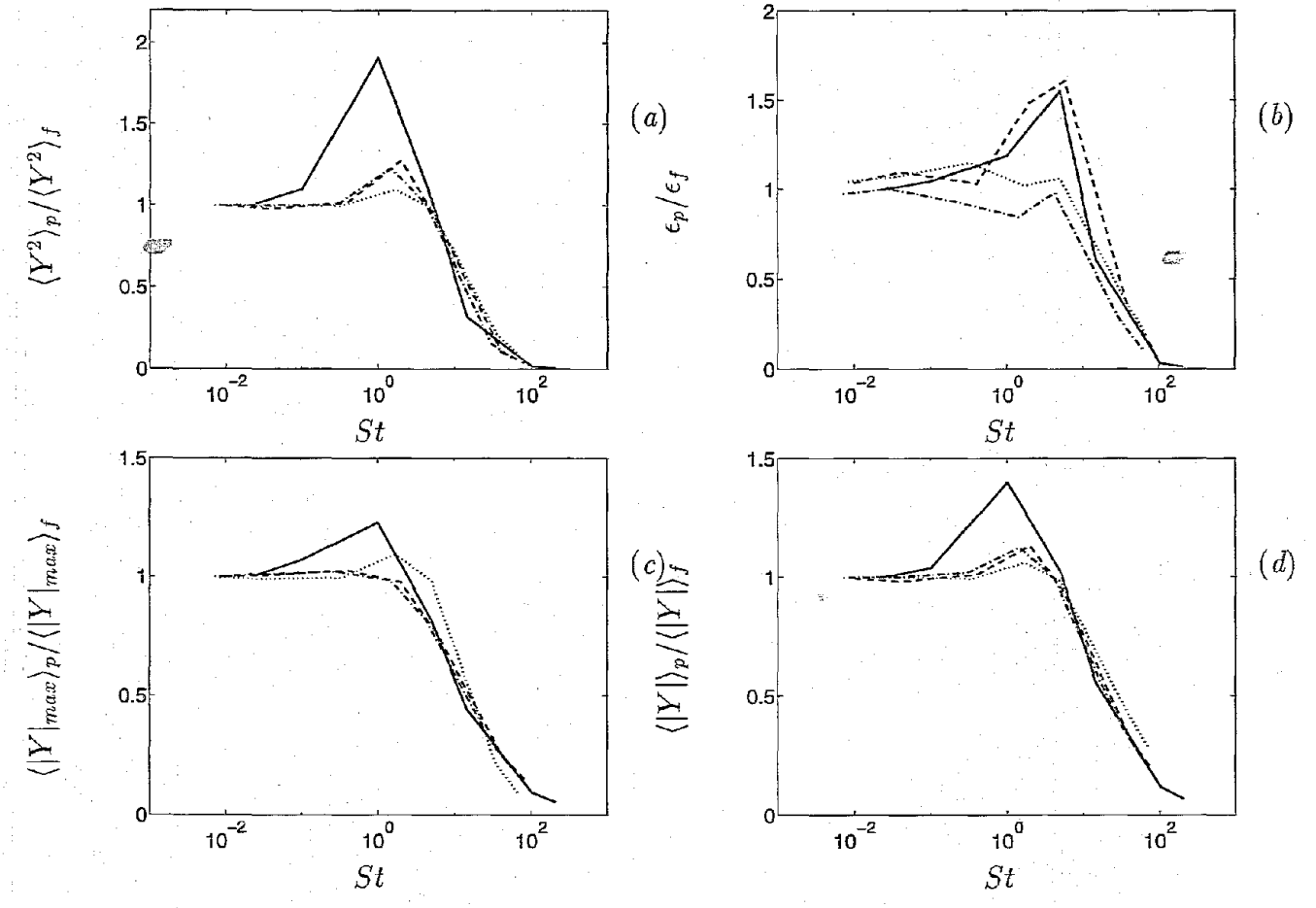

Figure 33: Measures of particle dispersion as a function of Stokes number defined using local vorticity thickness. —— $\tau = 108$; ---- $\tau = 216$; —·— $\tau = 257$; ····· $\tau = 315$.